Astronomy & Astrophysics

Testing external photoevaporation in the σ-Orionis cluster with spectroscopy and disk mass measurements

K. Maucó[1],[⋆], C. F. Manara[1], M. Ansdell[2], G. Bettoni[3,4], R. Claes[1], J. Alcala[5], A. Miotello[1], S. Facchini[3],
T. J. Haworth [6], G. Lodato[3], and J. P. Williams[7]

[1] European Southern Observatory, Karl-Schwarzschild-Strasse 2, 85748 Garching bei München, Germany
   e-mail: kmaucoco@eso.org
[2] NASA Headquarters, 300 E Street SW, Washington, DC 20546, USA
[3] Dipartimento di Fisica, Universitá degli Studi di Milano, Via Giovanni Celoria 16, 20133 Milano, Italy
[4] Max-Planck Institute for Extraterrestrial Physics, Gießenbachstraße 1, 85748 Garching, Germany
[5] INAF – Osservatorio Astronomico di Capodimonte, via Moiariello 16, 80131 Napoli, Italy
[6] Astronomy Unit, School of Physics and Astronomy, Queen Mary University of London, G O Jones Building, 327 Mile End Rd,
   Bethnal Green, London E1 4NS, UK
[7] Institute for Astronomy, University of Hawai'i at Mānoa, 2680 Woodlawn Dr, Honolulu, HI 96822, USA

ABSTRACT

Context. The evolution of protoplanetary disks is regulated by an interplay of several processes, either internal to the system or related to the environment. As most of the stars and planets, including our own Solar System, have formed in massive stellar clusters that contain OB-type stars, studying the effects of UV radiation on disk evolution is of paramount importance.

Aims. For this work, we tested the impact of external photoevaporation on the evolution of disks in the mid-age ($\sim$3–5 Myr) σ-Orionis cluster by conducting the first combined large-scale UV to IR spectroscopic and millimeter-continuum survey of this region.

Methods. We studied a sample of 50 targets located at increasing distances from the central, massive OB system σ-Ori. We combined new spectra obtained with VLT/X-shooter, used to measure mass accretion rates and stellar masses, with new and previously published ALMA measurements of disk dust and gas fluxes and masses.

Results. We confirm the previously found decrease in $M_{\rm dust}$ in the inner $\sim$0.5 pc of the cluster. This is particularly evident when considering the disks around the more massive stars ($\geq$0.4 $M_\odot$), where those located in the inner part ($<$0.5 pc) of the cluster have $M_{\rm dust}$ about an order of magnitude lower than the more distant ones. About half of the sample is located in the region of the $\dot{M}_{\rm acc}$ versus $M_{\rm disk}$ expected by models of external photoevaporation, namely showing shorter disk lifetimes than expected for their ages. The shorter disk lifetimes is observed for all targets with a projected separation from σ-Ori $<$ 0.5 pc, proving that the presence of a massive stellar system affects disk evolution.

Conclusions. External photoevaporation is a viable mechanism to explain the observed shorter disk lifetimes and lower $M_{\rm dust}$ in the inner $\sim$0.5 pc of the σ-Orionis cluster, where the effects of this process are more pronounced. Follow-up observations of the low stellar mass targets are crucial to constrain disk dispersion timescales in the cluster and to confirm the dependence of the external photoevaporation process with stellar host mass. This work confirms that the effects of external photoevaporation are significant down to at least impinging radiation as low as $\sim$10^4 G_0.

Key words. protoplanetary disks – accretion, accretion disks – stars: pre-main sequence – stars: variables: T Tauri, Herbig Ae/Be

1. Introduction

Protoplanetary disks, made of gas and dust, are the byproduct of the star formation process and are the places where planets form. Their evolution is mediated by the interplay of several physical processes most likely acting simultaneously, which makes understanding disk evolution challenging (Manara et al. 2023, for a review). The standard theory is framed in the steady-state viscous paradigm, where the transfer of angular momentum in the disk drives its evolution, and results in accretion onto the central star (e.g., Hartmann et al. 2016). Dispersal mechanisms, such as winds and outflows, also contribute to the evolution through the depletion of disk material (e.g., Frank et al. 2014; Ercolano & Pascucci 2017; Winter & Haworth 2022; Pascucci et al. 2023). Mass loss processes can have an internal origin, such

as inside-out clearing produced by the ionizing radiation of the host star, or come from an external source, for example, the local environment. Dynamical interactions between stars and external photoevaporation, driven by high-energy radiation fields from OB massive stars, are among the most commonly discussed processes affecting disk evolution in clustered environments (e.g., Winter et al. 2018; Reiter & Parker 2022; Cuello et al. 2023).

Given the variety of properties found in planetary systems in our Galaxy, the way forward for understanding disk evolution must include the analysis of general disk and host star properties measured in a large statistical sample of systems at different evolutionary stages and environments. This makes it possible to identify correlations between the parameters (e.g., disk mass, disk radii, and mass accretion rates) and their possible connection with the age of the region or its environment. Thanks to the availability of sensitive, wide-band optical spectrographs, such as the X-Shooter instrument on the Very Large Telescope (VLT), and radio interferometers, such as the Atacama Large

---

Millimeter and sub-millimeter Array (ALMA), it is now possible to measure some of these general properties (Miotello et al. 2023, for a review). In particular, the mass accreted onto the central star per unit time ($\dot{M}_{acc}$), drawn from UV-optical spectra, and the disk mass (M_{disk}), from ALMA observations, have proven to be very useful for this task (Manara et al. 2023). For instance, surveys of young stars in different star-forming regions (SFRs) have found a tentative trend of decreasing $\dot{M}_{acc}$ with age (e.g., Sicilia-Aguilar et al. 2010; Antoniucci et al. 2014; Briceño et al. 2019; Manzo-Martínez et al. 2020), predicted by viscous evolution models (e.g., Lynden-Bell & Pringle 1974; Hartmann et al. 1998). This observational trend, however, has large uncertainties, mainly due to unreliable age estimates for individual stars (e.g., Soderblom et al. 2014) and correlated uncertainties between stellar properties and estimated individual ages (Da Rio et al. 2014). Finally, an unexpectedly large fraction of high accretors are found in old (>5 Myr) regions (Ingleby et al. 2014; Manara et al. 2020, 2021; Testi et al. 2022).

Furthermore, measurements of M_{disk} (estimated from dust emission and assuming a gas-to-dust ratio of 100) are now available for large samples of disks (e.g., Ansdell et al. 2017, 2016; Pascucci et al. 2016; Barenfeld et al. 2016; Grant et al. 2021; van Terwisga & Hacar 2023), which, in combination with $\dot{M}_{acc}$, has allowed us to connect what is happening in the innermost regions ($\lesssim 1$ au) with outer disk properties and thus test disk evolution models. According to viscous evolution, $\dot{M}_{acc}$ should positively correlate with M_{disk} (predicted from the gas mass) in such a way as to expect a tighter correlation at older ages (Rosotti et al. 2017; Lodato et al. 2017; Somigliana et al. 2022). The $M_{disk}-\dot{M}_{acc}$ relation has now been empirically established for nearby SFRs, although with a (puzzling) large spread regardless of the age of the region (e.g., Manara et al. 2016b, 2020; Mulders et al. 2017), pointing to a deviation from the purely viscous evolution theory, possibly toward a further importance of magnetohydrodynamic (MHD) winds in driving accretion in the disk (Somigliana et al. 2023; Manara et al. 2023; Tabone et al. 2022).

However, these studies have mainly focused on nearby (<300 pc) low-mass SFRs that distinctly lack OB stars (e.g., Taurus, Andrews et al. 2013), and do not represent the environment where most planets have formed or the birth environment of our Solar System (e.g., Lada & Lada 2003; Fatuzzo & Adams 2008; Adams 2010; Winter et al. 2020). Given the increasing relevance attributed to environmental factors in modulating disk evolution and planet formation, several authors have now included the effects of external photoevaporation by massive stars in models of viscous disk evolution (e.g., Clarke 2007; Anderson et al. 2013; Facchini et al. 2016; Haworth et al. 2018; Sellek et al. 2020a; Coleman & Haworth 2022). The ratio $M_{disk}/\dot{M}_{acc}$ has gained particular attention as a proxy of disk evolution, and as a possible discriminant between external effects and other internal disk evolution mechanisms. Rosotti et al. (2017) showed that externally irradiated disks show a $M_{disk}/\dot{M}_{acc}$ ratio significantly lower than the expected value for a given system age, due to the radical disk mass depletion characteristic of this scenario. Similarly, external truncation in multiple stellar systems leads to a similar decrease in $M_{disk}/\dot{M}_{acc}$ (Zagaria et al. 2022).

An ideal region to test these aforementioned predictions is the σ-Orionis cluster. Its intermediate age (~ 3–5 Myr, Oliveira et al. 2004; Hernández et al. 2014) makes it young enough to remain bound, yet old enough for its central OB system (σ-Ori, Caballero 2007) to have left its imprint. In contrast to the Orion proplyds (O'dell et al. 1993), which are the most extreme examples of externally irradiated disks and on which

extreme ultraviolet (EUV) photons drive mass loss and shape the proplyds in close proximity (<0.03 pc) to θ^1 Ori C (Johnstone et al. 1998), the dispersal of disks in σ-Orionis is controlled by far-UV (FUV) radiation (e.g., Adams et al. 2004; Facchini et al. 2016; Haworth et al. 2018) as a result of the lower mass of its OB system (compared to θ^1 Ori C) and the larger separation of the stars to the center, depleting the disks close to σ-Ori. This was shown in the ALMA survey of σ-Orionis (Ansdell et al. 2017), which found a dearth of massive ($M_{dust} > 3 M_{\oplus}$) disks close (<0.5 pc) to the central OB stars, and a smooth distance-dependent trend in the disk dust mass distribution, in line with previous results in the NGC2024 and the Orion nebula clusters (Mann et al. 2014, 2015), and in other less massive regions in Orion (van Terwisga & Hacar 2023). This observed depletion of disk masses in σ-Orionis was later reproduced using external photoevaporative models (Winter et al. 2020). However, several other effects are at play, including dynamics in the clusters, and this trend could be coincidental (Parker et al. 2021).

Just measuring disk dust masses is not enough to firmly assess the effects of external photoevaporation on disk evolution in massive star-forming regions. Two additional observational probes can be used. The ratio of forbidden emission lines is also a way to detect signs of externally photoevaporated disks. Rigliaco et al. (2009) used this probe to claim that the SO587 disk in σ-Orionis is currently being externally photoevaporated, and this has also been supported by photoevaporative models recently (Ballabio et al. 2023). Additional forbidden emission line data analyzed by Gangi et al. (2023) for three targets in the σ-Orionis cluster are, however, still not conclusive telltale tests of external photoevaporation, both due to the strong nebular contamination and the small sample. The other observational proxy of external photoevaporation, the correlation between M_{disk} and $\dot{M}_{acc}$, has not yet been well established due to the lack of accurate mass accretion rates for sources with detected submillimeter fluxes. Previous estimates of accretion rates for σ-Orionis members were obtained either for a small subsample of very low-mass stars (Rigliaco et al. 2012) or using indirect tracers such as U-band photometry (Rigliaco et al. 2011) or the Hα line from low-resolution spectroscopy (Maucó et al. 2016). Therefore, this latter proxy has been used for the first time for this work for the σ-Orionis cluster.

Here, we present the results of the first large-scale spectroscopic survey of disk-bearing stars in the σ-Orionis cluster in which mass accretion rates are analyzed together with new and previously published disk masses. Our main objective is to study, for the first time, the relationship between $\dot{M}_{acc}$ and M_{disk}, and to further constrain the dependence of M_{disk} with the distance from the massive system σ-Ori. After describing the sample in Sect. 2 and the observations and data reduction in Sect. 3, we present our results on stellar parameters, and disk mass estimates in Sect. 4. We discuss the implications of our findings in the context of external photoevaporation in Sect. 5. Finally, we summarize our conclusions in Sect. 6.

2. Sample

The σ-Orionis cluster is located in the Orion OB1 association, which is one of the largest and nearest OB associations spanning over 200 deg^2 on the sky (see the review in Reipurth 2008). Their OB stars were first recognized by Garrison (1967) as a group of 15 B-type stars around the massive hierarchical triple system σ-Ori, whose most massive component is an O9.5V star (Caballero 2007; Simón-Díaz et al. 2015), shaping the photodisociation region known as the Horsehead Nebula
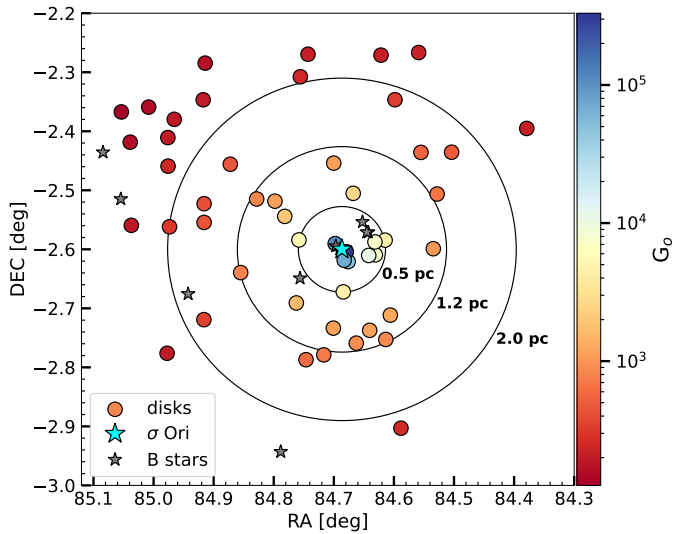
Fig. 1. Spatial distribution of σ-Orionis sources (points), and massive O-B stars (star symbols) in the cluster. The massive, multiple system σ-Ori is indicated in cyan while the rest of the B-type stars in gray. The color bar shows the incident FUV field strength (in terms of the dimensionless parameter G_o) due to the massive stars. Black circles show projected distances of 0.5, 1.2, and 2.0 pc.

(e.g., Abergel et al. 2003; Pety et al. 2005) and setting the UV field strength in the cluster (see Fig. B.1). In the last decades, several hundred low-mass stars and brown dwarfs have been already identified as part of the cluster (e.g., Reipurth 2008). The disks around the low-mass stars were first identified using *Spitzer* photometry (Hernández et al. 2007; Luhman et al. 2008) and then followed with *Herschel* (Maucó et al. 2016) and, more recently, imaged with ALMA at 1.3 mm (Ansdell et al. 2017) and followed down to the brown dwarf limit (Damian et al. 2023a,b). The low reddening toward its center (E(B-V) $\lesssim$ 0.1 mag, e.g., Brown et al. 1994; Béjar et al. 1999; Sherry et al. 2008) makes it an excellent natural laboratory to study protoplanetary disk evolution in the entire range of stellar masses and in the context of externally irradiated disks in moderate-to-high UV environments.

Our X-Shooter sample consists of 50 disk-bearing stars in the σ-Orionis cluster with ALMA observations (Ansdell et al. 2017) and located at different projected distances from σ-Ori (see Fig. 1). Of the 50 stars observed with X-Shooter, 43 have been detected by ALMA. The sample includes the objects studied in Rigliaco et al. (2012, 2009), and mainly consists of late-K and M spectral type (SpT) stars at different evolutionary stages based on the classification of their spectral energy distribution (SED, Luhman et al. 2003), as reported by Hernández et al. (2007), Rigliaco et al. (2011), Maucó et al. (2016). Our sample includes five disks with central cavities or transition disks (TD), one class I star (SO1153), which in the Luhman et al. (2003) classification points to a strong IR excess rather than to an embedded object (this source is visible at UV-optical wavelengths), and the rest are class II stars. The list of the observed targets is reported in Table A.1.

The *Gaia* EDR3 astrometric solutions for the sample are generally good, with low renormalized unit weight errors (RUWE). Only eight targets (SO397, SO490, SO563, SO583, SO587, SO736, SO823, and SO897) have RUWE values >1.4, considered an appropriate nominal limit for *Gaia* EDR3 (Gaia Collaboration 2021). For all targets, we assumed the individual distances inverting the parallaxes from *Gaia* EDR3

(arithmetic distances, Gaia Collaboration 2021). We then estimated the average distance to the cluster, considering only sources with RUWE <1.4, and found a median distance of 401 pc. This is compatible with the values reported by Damian et al. (2023b). Therefore, for all our targets we assumed their arithmetic distances unless the values were unreliable – RUWE >1.4 and/or distance differing more than 60 pc from the mean distance to the region (target SO936) – or not available (targets SO435, SO562, and SO1155), in which case we assumed the median distance to the members of the region. Distances for the sample are also listed in Table A.1.

Through this analysis, we found four targets, namely SO73, SO299, SO411, and SO848, whose distances are lower than the median by ~40 pc and yet have RUWE values <1.4. These can be possible members of the sparser Orion OB1a sub-association in front of σ-Orionis (Briceño et al. 2019). For SO411, this seems to be the case based on its proper motions (Pérez-Blanco et al. 2018); however, for the rest of these stars, we cannot know for certain. Therefore, we have included them in the analysis assuming their arithmetic distances from *Gaia*, and we have pointed them out whenever they appear as outliers from the main population. Similarly, the star SO828 with a distance of 449.5 pc (i.e., ~50 pc away from the median distance to the members of the region) is treated in the same way.

3. Observations and data reduction

3.1. Spectroscopy with VLT/X-shooter

Observations were carried out between October 2019 and February 2020 (Pr.Id. 0104.C-0454(A), PI Ansdell) and between November 2021 and January 2022 (Pr.Id. 108.22CB.001, PI Ansdell) in Service Mode at the ESO VLT. The X-Shooter instrument (Vernet et al. 2011) was used for all observations. This instrument acquires spectra simultaneously in three arms: UVB ($\lambda \sim$ 300–550 nm), VIS ($\lambda \sim$ 500–1050 nm), and NIR ($\lambda \sim$ 1000–2500 nm). All the stars were observed with a nodding pattern using a set of narrow slits (1.0″–0.4″–0.4″ in the UVB–VIS–NIR arms, respectively), yielding the highest spectral resolution (~5400, 18 400, 11 600, respectively). For flux calibrating the spectra, a short (~1 min to 10 min depending on target brightness) exposure in stare with a set of wide slits (5.0″) prior to the science exposure was taken.

Data reduction was done using the X-Shooter pipeline v.3.2.0 (P104 data) and v.3.5.0 (P108 data) (Modigliani et al. 2010) run within the ESO Reflex environment (Freudling et al. 2013) using the same procedure as in previous similar analyses (e.g., Alcalá et al. 2017; Manara et al. 2020; Venuti et al. 2019). The pipeline runs the classical reduction steps, including bias subtraction, flat-fielding, wavelength calibration, flexure and atmospheric dispersion correction, background removal (in stare mode) or combination of spectra obtained in a nodding cycle, and the extraction of the 1D spectrum. Telluric correction was then performed on the high-resolution spectra with the molecfit tool (Smette et al. 2015), which models the telluric absorption lines on the observed spectra using information on the atmospheric conditions in the night. Finally, the high-resolution spectra were rescaled to those obtained with the wider slit in order to account for slit losses and obtain absolute flux calibration. This methodology leads to accurate flux calibration of the spectra (e.g., Manara et al. 2021).

Particular care was taken in the case of the resolved binary system SO1267, where the two traces of the two targets, separated by 1.4″, were manually extracted using the IRAF software.

Throughout this paper, the source indicated as SO1267 refers to SO1267A. For the targets observed on nights with humidity higher than ~40% or with PWV ~9.5 mm, we did use the flux standard observed in the closest night with optimal conditions, to avoid introducing incorrect shapes in the NIR arm of the spectra. Finally, for SO844 and SO1154 we did rescale the narrow slit spectra to nonsimultaneous photometric data, since the wide slit spectra had non-reliable fluxes lower than the narrow slit ones, possibly due to the presence of thin cirrus at the time of the observations.

3.2. ALMA cycle 4 data

In this paper we use new, higher sensitivity Band 6 Cycle 4 ALMA observations obtained with eight Execution Blocks (EBs) on 29, 30 October 2016, 2, 3 November 2016, 14 May 2017, 2, and 4 July 2017 (Project ID: 2016.1.00447.S; PI: Williams). The array configuration used between 40 and 44 12m antennas, with baselines of ~20–2650 m in July 2017, leading to a spatial resolution of ~0.18″, and shorter baselines of ~15–1125 m in May 2017 and in 2016, with corresponding spatial resolution ~0.26″. The correlator setup included two broadband continuum windows centered on 234.3 and 216.5 GHz with bandwidths of 1.875 GHz and channel widths of 31.25 and 1.129 MHz, respectively. The bandwidth-weighted mean continuum frequency was 225.77 GHz (1.33 mm). The spectral windows covered the ^{12}CO (230.538 GHz), ^{13}CO (220.399 GHz), and $C^{18}O$ (219.560 GHz) $J = 2-1$ transitions at velocity resolutions of 0.079–0.096 km s^{-1}. These spectral windows had bandwidths of 58.59 MHz and channel widths of 60.6 kHz–0.071 MHz.

The raw data were pipeline calibrated at NRAO using the CASA package (version 4.7.2). The pipeline calibration included: absolute flux calibration with observations of J0522-3627 or J0423-0120; bandpass calibration with observations of J0510+1800 or J0522-3627; and gain calibration with observations of J0532-0307. We estimate an absolute flux calibration error of ~10% based on the amplitude variations of gain calibrators over time. The imaging of the continuum and line data was performed similarly to what was done by Ansdell et al. (2017), cleaning with a Briggs robust weighting parameter of 0.5. We find a median 1.33 mm continuum RMS of 50 μJy and the median ^{12}CO RMS is 11 mJy in 0.5 km s^{-1} channels. The achieved RMS for the Representative Window centered on ^{13}CO ($J = 2-1$) (220.399 GHz) is of 9.5 mJy beam^{-1} with a bandwidth of 0.096 km s^{-1} and a 0.30×0.22 arcsec beam, while the requested sensitivity was of 3.3 mJy^{-1} over 1.0 km s^{-1} and a beam size of 0.22 arcsec. The achieved continuum RMS is of 4.5×10^{-2} mJy beam^{-1} with a bandwidth of 3.4 GHz and a 0.27×0.19 arcsec beam. Continuum and ^{12}CO images are shown in Fig. D.2.

4. Results

4.1. Stellar and accretion properties

X-Shooter provides absolute flux calibrated spectra with sufficient spectral resolution and wavelength coverage to simultaneously characterize stellar, accretion, wind, jet, and ionization properties of young stellar objects (e.g, Bacciotti et al. 2011; Rigliaco et al. 2012; Alcalá et al. 2014; Frasca et al. 2017; Manara et al. 2016a, 2021). The continuum regions needed to determine stellar and accretion parameters range from $\lambda \sim 300$–364 nm (the Balmer continuum) to $\lambda \sim 700$ nm (where several molecular bands are present). Various absorption lines along
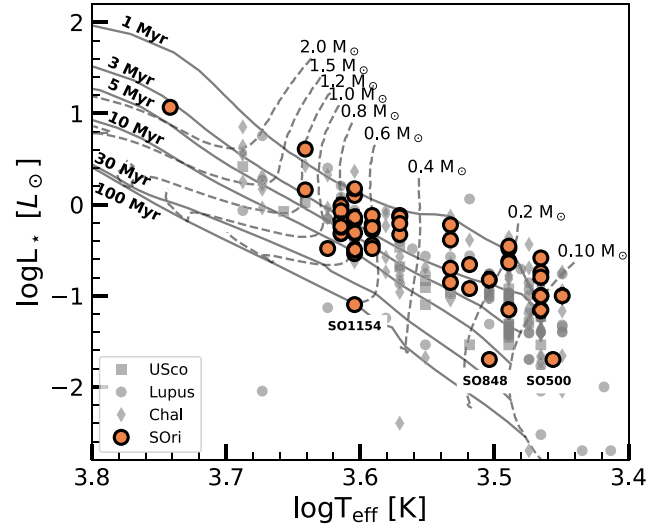

Fig. 2. Hertzsprung-Russell diagram for σ-Orionis disks (orange circles) including those from R12. Sources from other SFRs are shown by gray symbols. Isochrones for 1, 3, 5, 10, 30, and 100 Myr from Siess et al. (2000) are overplotted. Evolutionary tracks are from Baraffe et al. (2015).

the spectrum are required to constrain stellar spectral type and photospheric parameters (e.g., Manara et al. 2013a).

In order to derive the stellar and accretion properties of the targets, we follow the same fitting procedure as Manara et al. (2013a). In short, we model the spectra by adding a photospheric template spectrum plus a slab model to match the observed, dereddened spectrum. The grid of Class III photospheric templates includes targets with SpT from G- to late M taken from Manara et al. (2013b, 2017a), different slab models, and extinction values (A_V), assuming the Cardelli et al. (1989) reddening law ($R_V = 3.1$). The output from the models is the excess luminosity due to accretion (L_{acc}), given by the integrated flux of the best-fit slab models, and the stellar luminosity ($L_\star$), which is estimated by measuring the normalization of the Class III templates that best match the observations. Distances were estimated as described in Sect. 2. In Fig. E.1, we show the best-fit spectrum of each of our targets. We note that, as expected, A_V is typically low, reaching values above or equal to 1.0 mag only in 7 targets.

For the sake of comparison with other star-forming regions, we considered the same assumptions as Manara et al. (2023) and derived all the stellar and accretion parameters in a similar way. Therefore, we measure all luminosities ($L_\star$, L_{acc}) using the new *Gaia* distances and obtain T_{eff} from SpT using the calibration by Herczeg & Hillenbrand (2014). In Table A.2, we list the stellar and accretion parameters estimated for our sample, including those from the Rigliaco et al. (2012) sample, which are recalculated with the same assumptions that we just stated, including rescaling the distance from 360 pc to the *Gaia*-based ones.

Using the T_{eff} and $L_\star$ from the best-fit we were able to locate each target on the Hertzsprung–Russell diagram (HRD), as shown in Fig. 2. The targets in the σ-Orionis cluster are located in the region of the HRD consistent with their expected age (3–5 Myr). Three targets are located at lower $L_\star$ with respect to the bulk of the population at the same T_{eff}, namely SO500, SO848, and, SO1154. SO500 is a known brown dwarf (Rigliaco et al. 2011) and its location on the HRD is in line with other substellar objects. For SO1154, partial obscuration of the star by a highly inclined disk could explain their positions on the
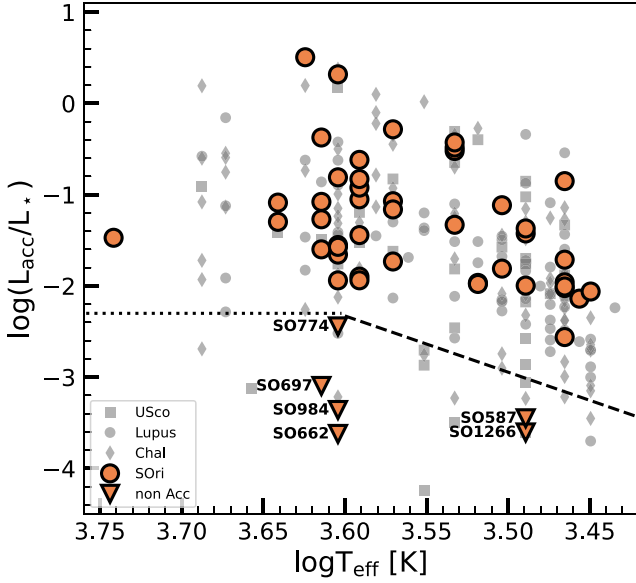
Fig. 3. Ratio between the accretion and stellar luminosities vs. effective temperature. σ-Orionis sources are indicated by orange circles while stars in other young SFRs by gray symbols. The dotted and dashed lines represent the locus of the chromospheric emission defined by Manara et al. (2013b, 2017a). Downward triangles indicate the non-accretors identified in this work.

HRD. A highly inclined disk can add gray extinction and make the star under-luminous, resulting in more uncertain estimates of $L_\star$ and of the mass accretion rate (Alcalá et al. 2014). This target is the one with the highest measured $A_V = 1.8$ mag, supporting the hypothesis of (partial) obscuration by a disk. Finally, SO848 could either also be a highly inclined disk, or a foreground object, as discussed in Sect. 2.

In order to check the estimates from the fit, we compared the values of $L_{\rm acc}$ obtained with the fitting procedure described above, with those derived from the luminosity of 10 emission lines, namely CaK, Hδ, Hγ, Hβ, HeI587 nm, Hα, HeI667 nm, Paγ, Paβ, Brγ, using the relations between line and accretion luminosity by Alcalá et al. (2017). The mean value of $L_{\rm acc}$ derived from the emission lines is generally in agreement with the one obtained by fitting the continuum in the X-Shooter spectrum with no dependence on the wavelengths of the lines, pointing toward correctly estimated A_V.

Figure 3 shows the ratio between accretion and stellar luminosities as a function of the effective temperature, which is a diagram used to check whether the measured accretion luminosity is larger than typical chromospheric emission (Manara et al. 2013a). Assuming the locus of chromospheric emission defined by Manara et al. (2017a), we found 6 non-accreting targets in our sample (downward triangles). As shown in Fig. E.1 these sources exhibit negligible UV excess, in line with their non-accreting nature. The rest of accreting targets have similar $L_{\rm acc}/L_\star$ values at any given $T_{\rm eff}$ as those found in other star-forming regions, in line with previous results.

After locating the targets in the HRD, we derive $M_\star$ using the nonmagnetic models of Baraffe et al. (2015) for colder stars ($T_{\rm eff} \leq 3900$ K), and of Feiden (2016) for hotter stars ($T_{\rm eff} > 3900$ K). For targets having stellar properties outside of the range of values sampled by these models, we used the Siess et al. (2000) models instead. Finally, the $\dot{M}_{\rm acc}$ is obtained from the classic relation $\dot{M}_{\rm acc} = 1.25 \times L_{\rm acc}R_\star/(GM_\star)$ from
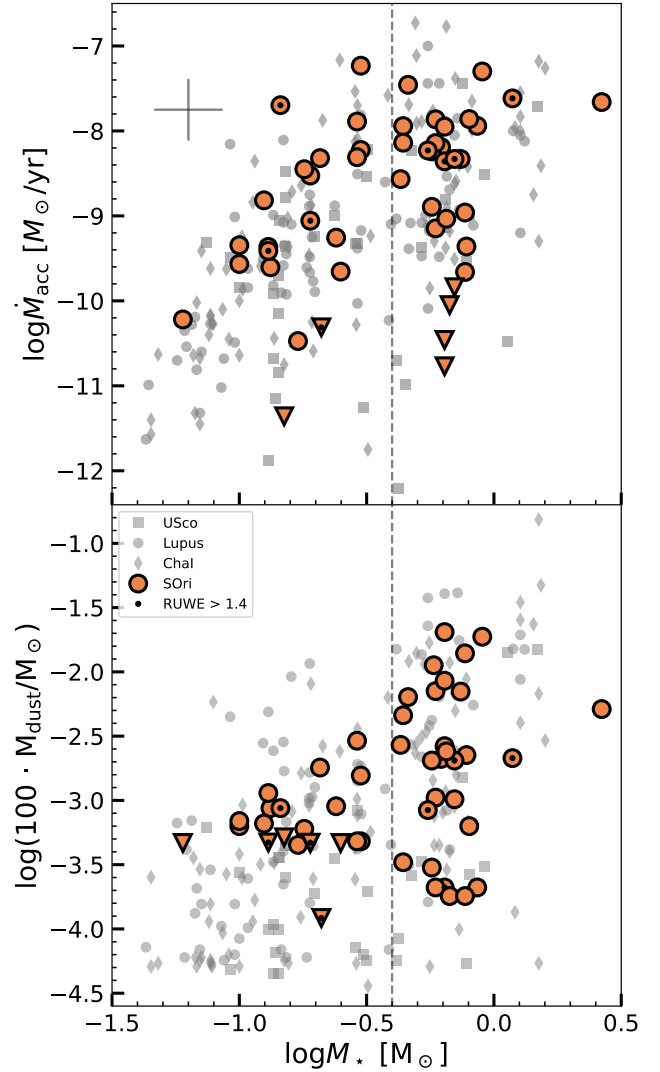

Fig. 4. Relations with stellar host mass. *Top:* mass accretion rates vs. stellar mass. The expected uncertainties are indicated by the error bars at the top left. *Bottom:* disk masses vs. stellar mass. All the targets from our sample and from Rigliaco et al. (2012) are plotted. Downward triangles indicate upper limits. The vertical dashed line indicates a $M_\star = 0.4\,M_\odot$.

Hartmann et al. (1998), using $L_{\rm acc}$ from the fit. The stellar and accretion parameters of the sample are found in Table A.2.

The relation between $\dot{M}_{\rm acc}$ and $M_\star$ is shown in Fig. 4 (top panel). Given the expected uncertainties on both quantities (error bar), the σ-Orionis disks seem to populate the same parameter space as the one covered by other young SFRs like Lupus, and Chameleon I, and even by the older (5–10 Myr; Pecaut & Mamajek 2016) Upper-Scorpius (USco). This will be further discussed in Sect. 5.2.

4.2. Disk masses

The disk masses are estimated through their submm ALMA flux at 1.3 mm (band 6) from cycle 3 (C3, Ansdell et al. 2017) and, when available, from our new, deeper ALMA observations taken in cycle 4 (C4) and reported here (Sect. 3.2). ALMA continuum fluxes are estimated as in Ansdell et al. (2017), that is by fitting point-source models to the visibility data using the *uvmodelfit* routine in *CASA*. More information on the ALMA
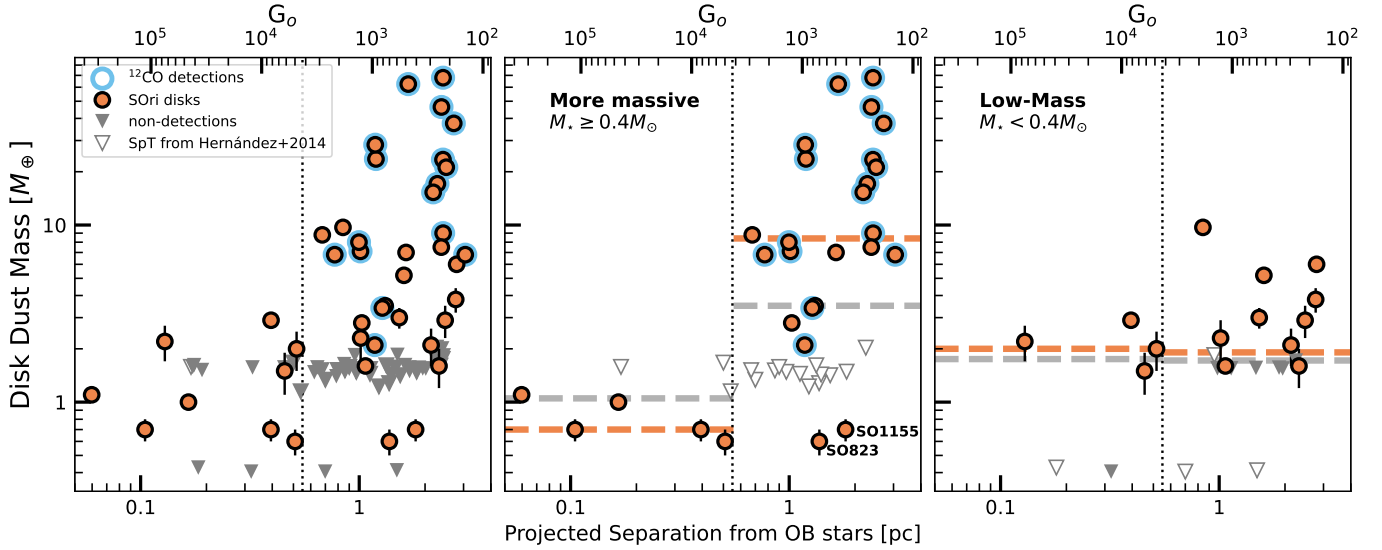
Fig. 5. Disk dust mass (M_{dust}) as a function of projected separation from σ-Ori. *Left:* considering the whole sample of disks with ALMA observations. *Middle:* considering the more massive ($M_\star \geq 0.4\,M_\odot$) stars in our σ Orionis sample. *Right:* considering the less massive ones ($M_\star < 0.4\,M_\odot$). Dashed lines show the M_{dust} median inside and outside 0.5 pc for our X-Shooter sample (orange) and also including upper limits with reported SpT in Hernández et al. (2014) (gray). Orange points are continuum detections, downward triangles are 3σ upper limits and, ^{12}CO detections (3σ) are indicated by an additional blue circle. The ^{12}CO fluxes are listed in Table A.2.

data is reported in Appendix D.1, which includes the comparison between ALMA fluxes from C3 and C4 observations in Fig. D.1. The measured fluxes are reported in Table A.2. In total, we have six new continuum detections from the C4 observations. These continuum fluxes were converted to dust masses taking into account the same assumptions as Manara et al. (2023) namely, following Ansdell et al. (2016), we used a prescription for the opacity, $\kappa_\nu = 2.3(\nu/230\,\text{GHz})\,\text{cm}^2\,\text{g}^{-1}$, taken from Beckwith et al. (1990). We used a single dust temperature, $T_{dust} = 20$ K, which has been empirically demonstrated to be a good disk-average value (Tazzari et al. 2021). The total disk mass is then obtained by multiplying the M_{dust} by a gas-to-dust ratio of 100. We rescaled the dust masses of Ansdell et al. (2017), which were estimated assuming $d = 385$ pc. The rescaled dust masses and their errors are reported in Table A.2.

The dependence of M_{dust} with the stellar mass is reported in Fig. 4, and shows a similar trend of increasing dust mass with stellar mass as in other star-forming regions, although with a large spread at $M_\star > 0.4\,M_\odot$ (vertical dashed line). We do not attempt a fit of the relation as in Ansdell et al. (2017), as we describe in Sect. 5.2 how we think that, in σ-Orionis, the spread is possibly a consequence of external photoevaporation.

We do not attempt to derive disk gas masses from the new detections of ^{12}CO in the C4 data. However, we will use the fluxes of ^{12}CO, measured as in Ansdell et al. (2017) using a curve-of-growth method on the moment 0 maps for the detected targets. In total, the C4 data lead to 13 new ^{12}CO detections. More information is provided in Appendix D.1.

5. Discussion

5.1. Dependence of disk mass with projected separation (and UV flux) from σ-Ori

As discussed in Ansdell et al. (2017), a dearth of massive ($M_{dust} > 3\,M_\oplus$) disks close (<0.5 pc) in projected distance to

the central O9 star σ-Ori was found in the σ-Orionis region, together with a shallow distance-dependent trend in disk dust mass. This result, similarly found in Mann et al. (2014, 2015) for other clusters in Orion, suggested that external photoevaporation may be a viable mechanism for disk depletion. In this work, we have included deeper ALMA data with 6 new detections (see Sect. 3.2). The updated M_{dust} distribution as a function of the projected separation from σ-Ori is shown in Fig. 5. We confirm the lack of any disk more massive than $\sim 3 M_\oplus$ in the inner ~ 0.5 pc of the cluster, and again a shallow distance-dependent trend of M_{dust}. The new detections further reinforce the limit in the inner part of the cluster, with detections of disks as low mass as less than $1\,M_\oplus$, and even more stringent upper limits. This strengthens the claim that many disks close to the ionizing star σ-Ori have extremely low masses due to its irradiation.

To further quantify the level at which σ-Ori affects the stars, we calculate the FUV radiation field strength due to the central OB system (see Appendix B for details). This is dominated by the radiation of σ-Ori alone. The top axis of Fig. 5 reports this FUV radiation strength expressed in terms of the Habing unit G_0 ($G_0 = 1.6 \times 10^{-3}$ erg cm^{-2} s^{-1}, Habing 1968). The range of FUV values for this region is between 10^2 and $10^5\,G_0$, lower than what is usually observed in the Orion Nebula Cluster (e.g., Winter & Haworth 2022), but still significant. Indeed, previous findings suggested that even moderate FUV fields ($\geq 2 \times 10^3 G_0$) can drive significant disk mass loss (Facchini et al. 2016; Kim et al. 2016; Haworth et al. 2018), consistent with the observed trend. In particular, the radiation received by a disk at a projected separation of ~ 0.5 pc from σ-Ori is $\sim 10^4\,G_0$, and in this range, the disks are found to have severely lower disk masses than at larger distances. However, the most massive disks ($M_{dust} \gtrsim 10\,M_\oplus$) are found only at projected distances larger than ~ 1 pc, corresponding to FUV fields of $\sim 10^3\,G_0$. Moreover, the CO detections, reported in Fig. 5 as blue circles, are found only at projected distances larger than 0.5 pc, although in a much higher fraction than that reported by Ansdell et al. (2017), mainly thanks to the deeper observations of C4 that were focused on the disks around

higher-mass stars ($M_\star \geq 0.5\,M_\odot$) as they tend to have brighter millimeter emission.

At this lower FUV field strength than the Orion Nebula Cluster or other massive regions, σ-Orionis is thus offering us the unique possibility to study external photoevaporation even at ~3–5 Myr, where the effects are clearly detectable but the disks are not yet (all) dispersed. We note that the observed distance-dependent depletion of disks has been reproduced using external photoevaporative models (Winter et al. 2020), although with overestimated (by a factor of 2) disk dust masses. Although, according to Parker et al. (2021), this could be coincidental, it is interesting to report on this new observational result to further constrain the models. Additional information to further support the external photoevaporation hypothesis is then discussed in the next sections.

5.2. Relations with stellar host mass

Thanks to large surveys of young stars performed in various SFRs, global stellar and disk properties have been estimated revealing different relations between the various parameters. Among the well-established ones is that of the $\dot{M}_{\rm acc}$ vs. $M_\star$, with a steeper-than-linear relation roughly as a power law with exponent ~2 (e.g., Hillenbrand et al. 1992; Muzerolle et al. 2003; Natta et al. 2006), and reported spreads in $\dot{M}_{\rm acc}$ values of about 1–2 dex (e.g., Alcalá et al. 2014; Manara et al. 2016a, 2017b, 2023; Venuti et al. 2014, 2019; Hartmann et al. 2016). Recently, evidence of a double power-law fit of this relation has also been seen (Alcalá et al. 2017; Manara et al. 2017a), with a very steep relation for the lowest-mass stars ($M_\star < 0.2$–$0.3\,M_\odot$) with slope ~4.5 followed by a flatter relation (slope~1) at higher $M_\star$. The distribution of the measured $\dot{M}_{\rm acc}$ as a function of the $M_\star$ for σ-Orionis sources are shown in the top panel of Fig. 4. These values reveal a great similarity with those found in other SFRs, like Lupus (Alcalá et al. 2017), Chamaeleon I (Manara et al. 2017b), and even the older USco SFR (Manara et al. 2020). A flatter dependence of $\dot{M}_{\rm acc}$ on $M_\star$ seems to be present at the highest $M_\star$ even in our sample, suggesting that the broken power-law could be a better fit to the data, in line with previous studies.

The similar range of $\dot{M}_{\rm acc}$ as in other typically younger SFRs is at odds with the usually assumed decline of $\dot{M}_{\rm acc}$ with age, a prediction of viscous evolution (e.g., Hartmann et al. 1998). This is however nowadays observed in several regions, from Orion OB1 (Ingleby et al. 2014; Manara et al. 2021; Pittman et al. 2022), to TWA (Venuti et al. 2019), η-Cha (Rugel et al. 2018), or even in the 30 Dor region (De Marchi et al. 2017). The reason why disks can have such a high accretion rate for a time not compatible with the amount of mass accreted over their lifetime and the total available mass in the disk, is still the subject of discussion (e.g., Hartmann et al. 2006) and, it is possibly related with episodic accretion or other mechanisms (Manara et al. 2020) but, in our specific case, it could be a selection effect due to a combination of enhanced accretion due to the effects of external photoevaporation (Rosotti et al. 2017), and the focus on just the disks that are not fully dispersed yet. Similarly to other star-forming regions, a large scatter of $\dot{M}_{\rm acc}$ at any $M_\star$ is observed for the σ-Orionis sources. Such a spread has been demonstrated not to be due to accretion variability or other sources of uncertainty (e.g., Manara et al. 2023, for a review) and its origin remains an open question. As also shown in Rigliaco et al. (2012), Winter et al. (2020), we find a positive correlation between $\dot{M}_{\rm acc}$ and $M_\star$ and no correlation of $\dot{M}_{\rm acc}$ with proximity to σ-Ori.

The bottom panel of Fig. 4 shows another correlation also well established empirically for individual regions, the $M_{\rm dust}$ vs. $M_\star$ relation. Several works surveying different SFRs have shown that $M_{\rm dust}$ directly depends on $M_\star$ with a slope around 1.8–2.7 with the larger values describing the older Upper Scorpius region (Ansdell et al. 2016, 2017; Barenfeld et al. 2016; Pascucci et al. 2016; Manara et al. 2023), and holds down to the brown dwarf regime (e.g., Testi et al. 2016; Sanchis et al. 2021; Rilinger & Espaillat 2021). The steepening with age has been interpreted as faster evolution of dust around low-mass stars, whether as a result of more efficient conversion of millimeter grains into larger centimeter grains or more efficient radial drift. Interestingly, the dispersion around the relation is very similar in all the regions (~0.8 dex). In the case of the σ-Orionis cluster, we find similar results as Ansdell et al. (2017) with sources populating a similar locus on this plane as in other SFRs. We also find a large scatter in $M_{\rm dust}$ for a given stellar mass, particularly large around the more massive stars ($M_\star \geq 0.4\,M_\odot$) in our sample. Since the dispersion is present for all regions, regardless of age and environment, it has been acknowledged as an inherent property of disk populations resulting from the range of disk initial conditions and has been explained theoretically, by invoking a mixture of both the initial conditions and the evolutionary process (Pascucci et al. 2016; Pinilla et al. 2020). However, we think that the origin of this dispersion at high stellar masses ($M_\star \geq 0.4\,M_\odot$) is possibly related to the effects of the massive star σ-Ori on the surrounding disks, as we discuss in the next subsection.

5.3. The effect of stellar mass on the disk mass depletion

In the middle and right panels of Fig. 5, we show the distribution of $M_{\rm dust}$ as a function of projected separation from σ-Ori for stars with $M_\star \geq 0.4\,M_\odot$ and $M_\star < 0.4\,M_\odot$, respectively. Dashed lines indicate the median values of $M_{\rm dust}$ for sources inside and outside a projected distance of 0.5 pc from the position of σ-Ori. Since SpT estimates are available from Hernández et al. (2014) for a subsample of stars with $M_{\rm dust}$ upper limits (gray triangles on the left panel) and without X-shooter spectra (i.e., without stellar mass estimates), we have added them as white downward triangles on these panels. Our SpT estimates are in good agreement within the uncertainties with those reported in Hernández et al. (2014). The only three targets that deviate more than expected are two strong accretors (SO562, SO1075) and one highly extincted star (SO823). We assigned the objects with SpT earlier than M2 in the higher mass panel, and for later SpT to the lower mass panel. The choice is motivated by the correspondence between SpT and $M_\star$ found in the X-shooter sample. The $M_{\rm dust}$ medians taking into account these additional values are shown with a gray dashed line, while those estimated from the X-shooter sample alone are shown with an orange dashed line.

Looking at Fig. 5 we note that, within the inner 0.5 pc from σ-Ori, the more massive ($M_\star \geq 0.4\,M_\odot$) stars in σ-Orionis (middle panel), show $M_{\rm dust}$ about an order of magnitude lower than the more distant ones considering only the targets with measured $M_\star$ (orange dashed lines), or about 4 times lower when including those where only the SpT is measured (gray dashed lines), although, in this case, the median inside 0.5 pc is more uncertain given the less stringent upper limits. By contrast, low-mass stars ($M_\star < 0.4\,M_\odot$) have an apparent constant distribution of $M_{\rm dust}$, regardless of their distance from the ionizing stars (right panel). Even though this trend will still hold including the additional (~19) upper limits shown in the left panel for which no SpT nor $M_\star$ estimate exists (as these

upper limits are of the same order as our detections), this apparent flatness in the M_{dust} distribution for the low-mass stars in our sample is surely affected by the low numbers statistics in this stellar mass range, mainly due to the distance of the cluster ($d = 401$ pc) which makes it harder to survey low-mass stars with respect to closer star-forming regions. It could be, therefore, that there are more low-mass stars inside 0.5 pc that were not targeted in the ALMA surveys because they were not part of the initial *Spitzer* catalogs. If these are fainter at mm-wavelengths than our targets, the few low-mass objects that are detected in close proximity to σ-Ori could represent the high upper tail of the low-mass distribution. Deeper ALMA observations on these additional targets along with spectroscopic follow-up are needed in order to probe the apparent flatness of the M_{dust} distribution of the low-mass stars in σ-Orionis. At the same time, the lower median M_{dust} for the low-mass stars compared to the more massive ones in the outer part of the cluster (beyond 0.5 pc), is due to the known steep dependence of M_{dust} with $M_\star$ just discussed. It is possible, therefore, to ascribe the differences in the outer part of the cluster to other (internal) effects related to the evolution of disks as well (Pascucci et al. 2016; Pinilla et al. 2020).

The large difference between the median M_{dust} for the more massive stars inside and outside projected distances of 0.5 pc from σ-Ori points, instead, to environmental factors, like external photoevaporation, affecting the closest disks to σ-Ori, decreasing significantly their M_{dust}, as discussed in Sect. 5.1. We note that this discrepancy holds even considering the additional upper limits for targets without $M_\star$ estimates from the spectroscopy presented in this work (gray dashed lines). It is also important to note that this discrepancy can be even larger if the two outliers (SO823 and SO1155, see Sect. 2) are not taken into account. Although the disks in the low-mass sample are in general less massive, as expected due to their faster dust evolution, the median M_{dust} within the innermost region of the cluster is still lower for the high-mass star sample than for the low-mass star regime (see Fig. 5). It is worth discussing, therefore, why such an effect is observed.

A possible solution to this puzzling result could be that the effects of external photoevaporation depend on the stellar mass of the host star in a more complex fashion than what is typically assumed. Indeed, for the fact that the gravitational potential is stronger for higher-mass stars, it is usually assumed that photoevaporation is more effective around lower-mass stars. This however is a very simplistic assumption, since it is known that the disk radii depend on the stellar mass as well, albeit indirectly through the already mentioned dependence of the continuum flux with the disk radii, and the fact that the disk masses are measured from the continuum flux. If the relation between the disk radii and the stellar mass is not linear, then external photoevaporation should affect the disks in a different way depending on the (unperturbed) disk radius.

External photoevaporation would result in a lower disk mass obtained as a result of eroding the disk in the outer regions, at disk radii (R_{disk}) larger than the gravitational radius, defined as $R_{grav} = (GM_\star)/c_s^2$ in an isothermal system, where c_s is the sound speed (Winter & Haworth 2022), or even down to $0.15 \cdot R_{grav}$ (Adams et al. 2004), although with lower mass-loss rates. If disks are eroded by this process, we expect the disk radii to be typically smaller than R_{grav}. Unfortunately, the spatial resolution of our observations ($\sim 0.2'' \sim 80$ au, see Sect. 3.2) is not sufficient to properly resolve the disks. However, we obtain indirect estimates of the disk radii using the measured continuum flux, known to correlate with the disk dust radii (Tripathi et al. 2017; Andrews et al. 2018; Long et al. 2022), and the measured ^{12}CO fluxes,

which can be related to the disk gas sizes under the assumption that the emission is optically thick (e.g., Zagaria et al. 2023; Toci et al. 2023; Trapman et al. 2023). In the cases where the ^{12}CO is not detected, it is possible to extrapolate the gas radii from the dust radii assuming a ratio of 3, found here for the targets with both continuum and ^{12}CO detections, and typically found in other star-forming regions (e.g., Ansdell et al. 2018). We note that this procedure is based on several assumptions, and, in particular, the latter is most probably not valid in the case of external photoevaporation, which mainly affects the gaseous component of the disk, where we expect a lower gas-to-dust radii ratio.

Assuming $c_s = 1\,\mathrm{km\,s^{-1}}$ (which gives ~ 120 K in 1000 G_0 environment) as representative for our sample, we can compare the inferred disk radii with the inferred gravitational radii (R_{disk}/R_{grav}) for each target. Although with many caveats, this analysis results in disk radii that are always smaller than the gravitational radii for all the stars in the cluster, with the lowest ratios ($R_{disk}/R_{grav} < 0.1$) for disks around stars $M_\star > 0.4\ M_\odot$ and with projected separation from σ-Ori smaller than 0.5 pc, whereas they are larger in the outer part of the cluster. This is in line with the expectations of the imprint of external photoevaporation, with a stronger effect on the inner regions of the cluster. As shown in Adams et al. (2004), the mass-loss rate due to externally irradiated disks can still be significant even for disk radii much smaller than the gravitational radius, in particular for $R_{disk}/R_{grav} > 0.15$, as we found in the outer part of the cluster. This reinforces the claim that even at intermediate FUV radiation fields (1–1000 G_0) the effects of this process can have a significant impact on the evolution of protoplanetary disks (van Terwisga & Hacar 2023). However, we note that the dependence of M_{disk} with the distance from σ-Ori is not as steep as it would be expected from the results of van Terwisga & Hacar (2023). The disks around the lowest mass stars, however, seem to have a constant ratio $R_{disk}/R_{grav} \sim 0.4$ regardless of the distance to σ-Ori, which is a consequence of the flat distribution of fluxes (and disk dust masses) with projected distance from σ-Ori shown in Fig. 5.

With all the several assumptions of our approach, namely the dependence of continuum and gas emission with the disk radii, the ratio between gas and dust disk radii, and the sensitivity of the R_{disk}/R_{grav} ratio to the value assumed for c_s, our approach points to a different dependence of the effect of external photoevaporation with stellar host mass. This is particularly evident in the dependence of M_{disk} with the projected distance from σ-Ori (Fig. 5).

Our findings suggest that the large spread in the M_{disk}–$M_\star$ relation observed for disks around stars with $M_\star > 0.4\ M_\odot$ is an effect of the environment in the σ-Orionis cluster. If confirmed, this would shed new light on the evolution of the M_{disk}–$M_\star$ relation with age, which is mainly driven by the large scatter (e.g., Manara et al. 2023), leading to an interpretation where, at least for the mid-aged σ-Orionis region, the steepening of the relation is an effect of external photoevaporation. Work should be done in trying to properly measure disk radii in these systems, particularly around low-mass stars, to confirm whether they are less affected by external photoevaporation, or whether the different behavior with respect to the disks around higher-mass stars is due to other processes.

5.4. $\dot{M}_{acc}$–M_{disk} plane as a proxy of disk evolution

According to the disk viscous evolution framework, $\dot{M}_{acc}$ should directly correlate with M_{disk} (e.g., Hartmann et al. 1998; Rosotti et al. 2017; Lodato et al. 2017; Mulders et al. 2017;
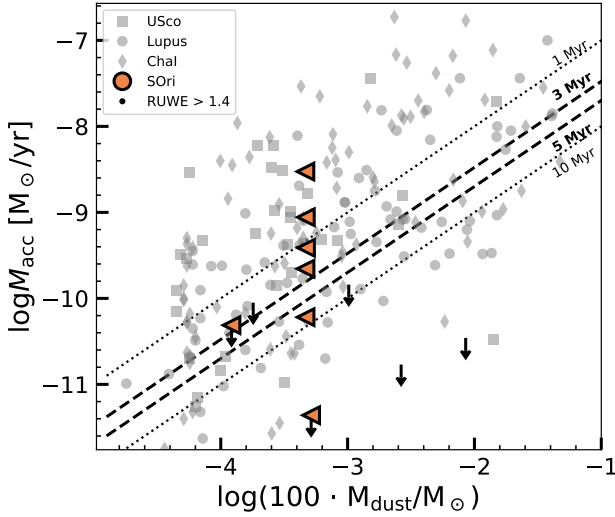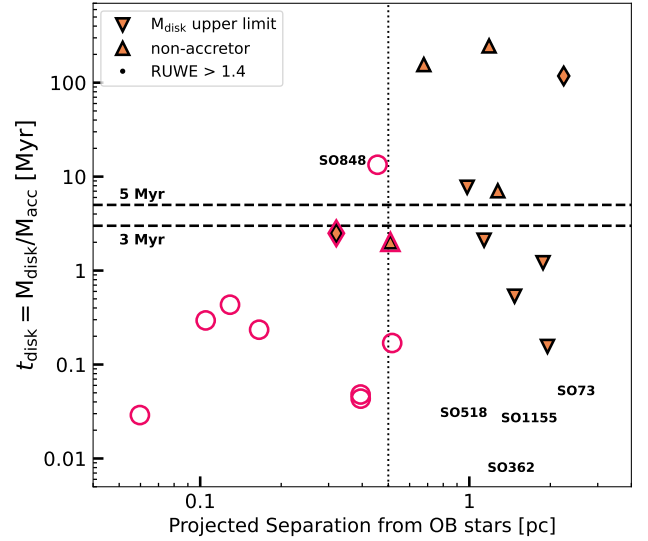
Fig. 6. Distribution of the $\dot{M}_{\rm acc}-M_{\rm disk}$ in σ-Orionis. The triangles indicate the upper limit on $M_{\rm disk}$, while the vertical arrows correspond to the upper limits on the $\dot{M}_{\rm acc}$. The dotted and dashed lines are the isochrones at some relevant ages. The ones in bold are related to the estimated age of the cluster, i.e., 3–5 Myr (Oliveira et al. 2004). Values for other star-forming regions (Manara et al. 2023) are shown as gray symbols for comparison.

Fig. 7. Distribution of $t_{\rm disk}$ as a function of projected separation from σ-Ori. The downward triangles indicate upper limits on $M_{\rm disk}$ while upward triangles indicate upper limits on $\dot{M}_{\rm acc}$. The vertical dotted line is located at 0.5 pc from σ-Ori. Targets within 0.5 pc are highlighted with an additional red outline. The dashed lines are related to the estimated age of the cluster, i.e., 3–5 Myr (Oliveira et al. 2004).

Manara et al. 2023). The viscous quasi-steady state is characterized by the condition $M_{\rm disk} \sim \dot{M}_{\rm acc}\tau$, with τ as the viscous timescale at the outer radius of the disk (Rosotti et al. 2017). One property of this paradigm is that τ is of the order of the system age independent of the initial conditions and the assumptions on disk viscosity (Jones et al. 2012; Lodato et al. 2017). Therefore, the ratio $M_{\rm disk}/\dot{M}_{\rm acc}$, the so-called "disk lifetime" ($t_{\rm disk}$) can be used as a proxy of disk evolution (Manara et al. 2016b, 2023; Rosotti et al. 2017). The dependence between $M_{\rm disk}$ and $\dot{M}_{\rm acc}$ has been explored extensively in the literature and found to be almost linear, albeit with a very large scatter (e.g., Manara et al. 2016b, 2020, 2023; Mulders et al. 2017).

The origin of the observed scatter at all ages is still unclear, although it points toward particular conditions in the viscous framework (Lodato et al. 2017), or to the necessity to include other mechanisms to explain the observations. Both Rosotti et al. (2017) and Zagaria et al. (2022) suggest that external disturbances, such as external photoevaporation or multiplicity, lead to shorter disk lifetimes, that is higher $\dot{M}_{\rm acc}$ than the value expected by viscous evolution corresponding to the measured disk mass. Zagaria et al. (2022) found that multiplicity can explain the high accretors found in the Upper Scorpius region (Manara et al. 2020).

The data presented in this work allows us, for the first time, to test whether the $\dot{M}_{\rm acc}$-$M_{\rm disk}$ relation can be used to confirm the effect of external photoevaporation on disks close to a massive star. Figure 6 shows the $\dot{M}_{\rm acc}-M_{\rm disk}$ plane for our σ-Orionis disk sample. We highlight the $t_{\rm disk}$ = 3 Myr and, 5 Myr (dashed lines), representative of the age of the cluster (Oliveira et al. 2004; Hernández et al. 2014), for reference. We observe that the majority of the targets are located at shorter disk lifetimes than the age of the region, in line with the expectations from external photoevaporation models (Rosotti et al. 2017). In particular, 28 targets (~54%) lay above the 1 Myr line, 17 targets (~34%) are between the 1 Myr and 10 Myr lines, while the remaining five targets (~10%) are below the 10 Myr line, and they are mainly non-accreting objects. This points toward confirming the effect of external photoevaporation on the evolution of these disks.

We note, however, that the distribution of data on the $\dot{M}_{\rm acc}$-$M_{\rm disk}$ plane is similar to what is observed in other SFRs. According to Zagaria et al. (2022), most of the stars in Lupus, Chameleon I, and USCo SFRs that have higher $\dot{M}_{\rm acc}$ given their $M_{\rm disk}$ can be explained by multiplicity (tidally truncated disks), with the bulk of the binary population being clustered around $M_{\rm disk}/\dot{M}_{\rm acc} = 0.1$ Myr. Unfortunately, we do not have multiplicity information for our σ-Orionis sample to further test this scenario, but we have indicated in the plots the stars with RUWE values greater than 1.4, which may point to possible binaries in the cluster. Interestingly, most of the targets with high RUWE have also short disk lifetimes, suggesting that binarity might play a role also in the σ-Orionis cluster in the observed spread in the $\dot{M}_{\rm acc}-M_{\rm disk}$ relation.

To further check whether the short disk lifetimes could be instead related to the presence of the massive σ-Ori star, we show in Fig. 7 how $t_{\rm disk}$ depends on the projected distance to the massive σ-Ori system. As shown, all objects within 0.5 pc from σ-Ori (red circles) have $t_{\rm disk} < 0.5$ Myr, while disks further out can reach higher values. Outliers, having $t_{\rm disk} < 0.05$ Myr at 1 pc or beyond, correspond to objects whose distances deviate in more than ~40 pc to the median (SO73, SO848), strong accretors (SO1155, SO362) and/or edge-on disks candidates (SO518). The low disk lifetimes of the disks closest to the OB stars along with the distance-dependent trend in disk dust mass shown in Fig. 5, robustly evidence the fact that, at least within 0.5 pc of the center, the disks are actively being externally photoevaporated.

The dependence of the disk lifetime with the projected separation from σ-Ori further suggests that, despite the similar distribution on the $\dot{M}_{\rm acc}-M_{\rm disk}$ plane as in other regions, the large spread observed in our σ-Orionis sample also supports the outside-in depletion of these disks. As stated in Lodato et al. (2017), from disk population synthesis models, a tighter $M_{\rm disk}-\dot{M}_{\rm acc}$ correlation is expected at longer ages, so the fact that these sources show a similar spread, even at these intermediate ages, to other younger SFRs implies a more significant deviation of these stars from purely viscous evolution. Enlarging the

sample on the low disk mass side, by adding additional disk detections to the available spectroscopic data, would constrain quantitatively how many disks are consistent with the effects of external photoevaporation, or whether other effects must be considered in order to explain the observations, such as the effects of dust evolution (e.g., Sellek et al. 2020b) or binarity (e.g., Zagaria et al. 2022).

6. Conclusions

We have conducted the first large-scale survey with both UV-to-NIR spectroscopy with X-Shooter, and millimeter interferometry with ALMA, for disk-bearing stars in the mid-age σ-Orionis cluster. We have derived the stellar and accretion properties of 50 targets, and shown new ALMA detections to complement the data presented by Ansdell et al. (2017). This has allowed us to test the effect of external photoevaporation from the massive star σ-Ori on the surrounding population of disks.

Our main conclusions are:

– The disks in the σ-Orionis cluster show similar values and spread in the $\dot{M}_{acc}$–$M_\star$ and M_{disk}–$M_\star$ relations as those in surveys of protoplanetary disks in other young SFRs. No correlation of $\dot{M}_{acc}$ with proximity to σ-Ori was found, in agreement with previous works.

– We confirm the trend of decreasing M_{dust} at shorter distances from the massive star σ-Ori, as expected from external photoevaporation. Disks around more massive stars show a more pronounced reduction in their masses if they are located in the inner 0.5 pc of the cluster than disks in the outer regions. They were also found to have the smallest R_{disk}/R_{grav} ratio at these separations, which corresponds to a value of FUV radiation of ~10^4 G_0. This effect is less pronounced in the lowest mass stars, either due to a stellar mass-dependent effect of external photoevaporation or to observational biases. Due to the low number statistics, the conclusions for the low-mass regime have yet to be firmly established. Our results stress the need to develop a deeper understanding of disk evolution around very low-mass stars in clustered environments.

– Half of the sample lies in the expected region for externally irradiated disks on the $\dot{M}_{acc}$ versus M_{disk} plane, showing a disk lifetime (t_{disk}) lower than expected given the age of the system. This implies that external photoevaporation may be a viable mechanism for disk depletion in the cluster.

– We found a tentative increasing trend of t_{disk} with the projected separation from the massive OB stars. Within the first 0.5 pc, sources have a very low t_{disk} (≤0.5 Myr). This strengthens the claim that outside-in depletion plays an important role in the evolution of disks, particularly those that are in close proximity (<0.5 pc) to the central OB system σ-Ori.

While this work has shown the power of combining information on disk properties with measurements of stellar and accretion parameters as a function of the projected separation from the massive OB-system σ-Ori, the final telltale test of external photoevaporation in this region is to detect the photoevaporating winds in these targets. A detailed study on wind tracers and mass-loss diagnostic (e.g., optical forbidden emission lines) of these sources using X-shooter and high-resolution spectra can potentially confirm the above result and put better constraints on disk dispersal mechanisms in clustered environments (e.g., Hasegawa et al. 2022). This has been attempted in a limited number of targets (Rigliaco et al. 2009; Gangi et al. 2023), and it will be assessed in a future paper (Maucó et al., in prep.).

References

Abergel, A., Teyssier, D., Bernard, J. P., et al. 2003, A&A, 410, 577
Adams, F. C. 2010, ARA&A, 48, 47
Adams, F. C., Hollenbach, D., Laughlin, G., & Gorti, U. 2004, ApJ, 611, 360
Alcalá, J. M., Natta, A., Manara, C. F., et al. 2014, A&A, 561, A2
Alcalá, J. M., Manara, C. F., Natta, A., et al. 2017, A&A, 600, A20
Anderson, K. R., Adams, F. C., & Calvet, N. 2013, ApJ, 774, 9
Andrews, S. M., Rosenfeld, K. A., Kraus, A. L., & Wilner, D. J. 2013, ApJ, 771, 129
Andrews, S. M., Huang, J., Pérez, L. M., et al. 2018, The Messenger, 174, 19
Ansdell, M., Williams, J. P., van der Marel, N., et al. 2016, ApJ, 828, 46
Ansdell, M., Williams, J. P., Manara, C. F., et al. 2017, AJ, 153, 240
Ansdell, M., Williams, J. P., Trapman, L., et al. 2018, ApJ, 859, 21
Antoniucci, S., García López, R., Nisini, B., et al. 2014, A&A, 572, A62
Bacciotti, F., Whelan, E. T., Alcalá, J. M., et al. 2011, ApJ, 737, L26
Ballabio, G., Haworth, T. J., & Henney, W. J. 2023, MNRAS, 518, 5563
Baraffe, I., Homeier, D., Allard, F., & Chabrier, G. 2015, A&A, 577, A42
Barenfeld, S. A., Carpenter, J. M., Ricci, L., & Isella, A. 2016, ApJ, 827, 142
Beckwith, S. V. W., Sargent, A. I., Chini, R. S., & Guesten, R. 1990, AJ, 99, 924
Béjar, V. J. S., Zapatero Osorio, M. R., & Rebolo, R. 1999, ApJ, 521, 671
Briceño, C., Calvet, N., Hernández, J., et al. 2019, AJ, 157, 85
Brown, A. G. A., de Geus, E. J., & de Zeeuw, P. T. 1994, A&A, 289, 101
Caballero, J. A. 2007, A&A, 466, 917
Calvet, N., & Gullbring, E. 1998, ApJ, 509, 802
Cardelli, J. A., Clayton, G. C., & Mathis, J. S. 1989, ApJ, 345, 245
Clarke, C. J. 2007, MNRAS, 376, 1350
Coleman, G. A. L., & Haworth, T. J. 2022, MNRAS, 514, 2315
Cuello, N., Ménard, F., & Price, D. J. 2023, Eur. Phys. J. Plus, 138, 11
Da Rio, N., Jeffries, R. D., Manara, C. F., & Robberto, M. 2014, MNRAS, 439, 3308
Damian, B., Jose, J., Biller, B., et al. 2023a, ApJ, 951, 139
Damian, B., Jose, J., Biller, B., & Paul, K. T. 2023b, J. Astrophys. Astron., 44, 77
De Marchi, G., Panagia, N., & Beccari, G. 2017, ApJ, 846, 110
Ercolano, B., & Pascucci, I. 2017, Roy. Soc. Open Sci., 4, 170114
Facchini, S., Clarke, C. J., & Bisbas, T. G. 2016, MNRAS, 457, 3593
Fatuzzo, M., & Adams, F. C. 2008, ApJ, 675, 1361
Feiden, G. A. 2016, A&A, 593, A99
Frank, A., Ray, T. P., Cabrit, S., et al. 2014, in Protostars and Planets VI, eds. H. Beuther, R. S. Klessen, C. P. Dullemond, & T. Henning, 451
Frasca, A., Biazzo, K., Alcalá, J. M., et al. 2017, A&A, 602, A33
Freudling, W., Romaniello, M., Bramich, D. M., et al. 2013, A&A, 559, A96

Gaia Collaboration (Brown, A. G. A., et al.) 2021, A&A, 649, A1
Gangi, M., Nisini, B., Manara, C. F., et al. 2023, A&A, 675, A153
Garrison, R. F. 1967, PASP, 79, 433
Grant, S. L., Espaillat, C. C., Wendeborn, J., et al. 2021, ApJ, 913, 123
Habing, H. J. 1968, Bull. Astron. Inst. Netherland, 19, 421
Hartmann, L., Calvet, N., Gullbring, E., & D'Alessio, P. 1998, ApJ, 495, 385
Hartmann, L., D'Alessio, P., Calvet, N., & Muzerolle, J. 2006, ApJ, 648, 484
Hartmann, L., Herczeg, G., & Calvet, N. 2016, ARA&A, 54, 135
Hasegawa, Y., Haworth, T. J., Hoadley, K., et al. 2022, ApJ, 926, L23
Haworth, T. J., Clarke, C. J., Rahman, W., Winter, A. J., & Facchini, S. 2018, MNRAS, 481, 452
Herczeg, G. J., & Hillenbrand, L. A. 2014, ApJ, 786, 97
Hernández, J., Hartmann, L., Megeath, T., et al. 2007, ApJ, 662, 1067
Hernández, J., Calvet, N., Perez, A., et al. 2014, ApJ, 794, 36
Hillenbrand, L. A., Strom, S. E., Vrba, F. J., & Keene, J. 1992, ApJ, 397, 613
Ingleby, L., Calvet, N., Hernández, J., et al. 2014, ApJ, 790, 47
Johnstone, D., Hollenbach, D., & Bally, J. 1998, ApJ, 499, 758
Jones, M. G., Pringle, J. E., & Alexander, R. D. 2012, MNRAS, 419, 925
Kim, J. S., Clarke, C. J., Fang, M., & Facchini, S. 2016, ApJ, 826, L15
Lada, C. J., & Lada, E. A. 2003, ARA&A, 41, 57
Lodato, G., Scardoni, C. E., Manara, C. F., & Testi, L. 2017, MNRAS, 472, 4700
Long, F., Andrews, S. M., Rosotti, G., et al. 2022, ApJ, 931, 6
Luhman, K. L., Stauffer, J. R., Muench, A. A., et al. 2003, ApJ, 593, 1093
Luhman, K. L., Hernández, J., Downes, J. J., Hartmann, L., & Briceño, C. 2008, ApJ, 688, 362
Lynden-Bell, D., & Pringle, J. E. 1974, MNRAS, 168, 603
Manara, C. F., Beccari, G., Da Rio, N., et al. 2013a, A&A, 558, A114
Manara, C. F., Testi, L., Rigliaco, E., et al. 2013b, A&A, 551, A107
Manara, C. F., Fedele, D., Herczeg, G. J., & Teixeira, P. S. 2016a, A&A, 585, A136
Manara, C. F., Rosotti, G., Testi, L., et al. 2016b, A&A, 591, L3
Manara, C. F., Frasca, A., Alcalá, J. M., et al. 2017a, A&A, 605, A86
Manara, C. F., Testi, L., Herczeg, G. J., et al. 2017b, A&A, 604, A127
Manara, C. F., Natta, A., Rosotti, G. P., et al. 2020, A&A, 639, A58
Manara, C. F., Frasca, A., Venuti, L., et al. 2021, A&A, 650, A196
Manara, C. F., Ansdell, M., Rosotti, G. P., et al. 2023, in Protostars and Planets VII, eds. S. Inutsuka, Y. Aikawa, T. Muto, K. Tomida, & M. Tamura, Astronomical Society of the Pacific Conference Series, 534, 539
Mann, R. K., Di Francesco, J., Johnstone, D., et al. 2014, ApJ, 784, 82
Mann, R. K., Andrews, S. M., Eisner, J. A., et al. 2015, ApJ, 802, 77
Manzo-Martínez, E., Calvet, N., Hernández, J., et al. 2020, ApJ, 893, 56
Maucó, K., Hernández, J., Calvet, N., et al. 2016, ApJ, 829, 38
Miotello, A., Kamp, I., Birnstiel, T., Cleeves, L. C., & Kataoka, A. 2023, in Protostars and Planets VII, eds. S. Inutsuka, Y. Aikawa, T. Muto, K. Tomida, & M. Tamura, Astronomical Society of the Pacific Conference Series, 534, 501
Modigliani, A., Goldoni, P., Royer, F., et al. 2010, SPIE Conf. Ser., 7737, 773728
Mulders, G. D., Pascucci, I., Manara, C. F., et al. 2017, ApJ, 847, 31
Muzerolle, J., Hillenbrand, L., Calvet, N., Briceño, C., & Hartmann, L. 2003, ApJ, 592, 266
Natta, A., Testi, L., & Randich, S. 2006, A&A, 452, 245
O'dell, C. R., Wen, Z., & Hu, X. 1993, ApJ, 410, 696
Oliveira, J. M., Jeffries, R. D., & van Loon, J. T. 2004, MNRAS, 347, 1327

Parker, R. J., Alcock, H. L., Nicholson, R. B., Panić, O., & Goodwin, S. P. 2021, ApJ, 913, 95
Pascucci, I., Cabrit, S., Edwards, S., et al. 2023, in Protostars and Planets VII, eds. S. Inutsuka, Y. Aikawa, T. Muto, K. Tomida, & M. Tamura, Astronomical Society of the Pacific Conference Series, 534, 567
Pascucci, I., Testi, L., Herczeg, G. J., et al. 2016, ApJ, 831, 125
Pecaut, M. J., & Mamajek, E. E. 2016, MNRAS, 461, 794
Pérez-Blanco, A., Maucó, K., Hernández, J., et al. 2018, ApJ, 867, 116
Pety, J., Teyssier, D., Fossé, D., et al. 2005, A&A, 435, 885
Pinilla, P., Pascucci, I., & Marino, S. 2020, A&A, 635, A105
Pittman, C. V., Espaillat, C. C., Robinson, C. E., et al. 2022, AJ, 164, 201
Reipurth, B. 2008, Handbook of Star Forming Regions, Volume I: The Northern Sky, 4
Reiter, M., & Parker, R. J. 2022, Eur. Phys. J. Plus, 137, 1071
Rigliaco, E., Natta, A., Randich, S., & Sacco, G. 2009, A&A, 495, L13
Rigliaco, E., Natta, A., Randich, S., Testi, L., & Biazzo, K. 2011, A&A, 525, A47
Rigliaco, E., Natta, A., Testi, L., et al. 2012, A&A, 548, A56
Rilinger, A. M., & Espaillat, C. C. 2021, ApJ, 921, 182
Rosotti, G. P., Clarke, C. J., Manara, C. F., & Facchini, S. 2017, MNRAS, 468, 1631
Rugel, M., Fedele, D., & Herczeg, G. 2018, A&A, 609, A70
Sanchis, E., Testi, L., Natta, A., et al. 2021, A&A, 649, A19
Sellek, A. D., Booth, R. A., & Clarke, C. J. 2020a, MNRAS, 498, 2845
Sellek, A. D., Booth, R. A., & Clarke, C. J. 2020b, MNRAS, 492, 1279
Sherry, W. H., Walter, F. M., Wolk, S. J., & Adams, N. R. 2008, AJ, 135, 1616
Sicilia-Aguilar, A., Henning, T., & Hartmann, L. W. 2010, ApJ, 710, 597
Siess, L., Dufour, E., & Forestini, M. 2000, A&A, 358, 593
Simón-Díaz, S., Caballero, J. A., Lorenzo, J., et al. 2015, ApJ, 799, 169
Smette, A., Sana, H., Noll, S., et al. 2015, A&A, 576, A77
Soderblom, D. R., Hillenbrand, L. A., Jeffries, R. D., Mamajek, E. E., & Naylor, T. 2014, in Protostars and Planets VI, eds. H. Beuther, R. S. Klessen, C. P. Dullemond, & T. Henning, 219
Somigliana, A., Toci, C., Rosotti, G., et al. 2022, MNRAS, 514, 5927
Somigliana, A., Testi, L., Rosotti, G., et al. 2023, ApJ, 954, L13
Tabone, B., Rosotti, G. P., Lodato, G., et al. 2022, MNRAS, 512, L74
Tazzari, M., Testi, L., Natta, A., et al. 2021, MNRAS, 506, 5117
Testi, L., Natta, A., Scholz, A., et al. 2016, A&A, 593, A111
Testi, L., Natta, A., Manara, C. F., et al. 2022, A&A, 663, A98
Toci, C., Lodato, G., Livio, F. G., Rosotti, G., & Trapman, L. 2023, MNRAS, 518, L69
Trapman, L., Rosotti, G., Zhang, K., & Tabone, B. 2023, ApJ, 954, 41
Tripathi, A., Andrews, S. M., Birnstiel, T., & Wilner, D. J. 2017, ApJ, 845, 44
van Terwisga, S. E., & Hacar, A. 2023, A&A, 673, A2
Venuti, L., Bouvier, J., Flaccomio, E., et al. 2014, A&A, 570, A82
Venuti, L., Stelzer, B., Alcalá, J. M., et al. 2019, A&A, 632, A46
Vernet, J., Dekker, H., D'Odorico, S., et al. 2011, A&A, 536, A105
Winter, A. J. & Haworth, T. J. 2022, Eur. Phys. J. Plus, 137, 1132
Winter, A. J., Clarke, C. J., Rosotti, G., et al. 2018, MNRAS, 478, 2700
Winter, A. J., Ansdell, M., Haworth, T. J., & Kruijssen, J. M. D. 2020, MNRAS, 497, L40
Zagaria, F., Clarke, C. J., Rosotti, G. P., & Manara, C. F. 2022, MNRAS, 512, 3538
Zagaria, F., Facchini, S., Miotello, A., et al. 2023, A&A, 672, A15

Appendix A: Tables

Table A.1 lists the observed targets with their distances and UV field strengths. Table A.2 lists the stellar and accretion parameters as well as their continuum and ^{12}CO fluxes and dust masses estimated for our sample.

Appendix B: UV radiation field strength

We estimated the FUV radiation field strength due to the central OB system σ-Ori. For this, we followed the same approach as Winter & Haworth (2022). We considered the three most massive stars in the hierarchical system σ-Ori: σ Ori Aa ($M_\star = 20$ $M_\odot$), σ Ori Ab ($M_\star = 14.6$ $M_\odot$), and σ Ori B ($M_\star = 13.6$ $M_\odot$) from Simón-Díaz et al. (2015), and using Fig. 14 of Winter & Haworth (2022) we estimated the FUV luminosity ($L_{\rm FUV}$) of the system. The FUV field strength due to the massive OB stars was then obtained in terms of the dimensionless parameter G_0 as:

$$G_0 = \frac{1}{F_0} \frac{L_{\rm FUV}}{4\pi d_p^2},\tag{B.1}$$

where F_0 is the typical interstellar flux level of 1.6×10^{-3} erg cm^{-2} s^{-1} (Habing 1968), and d_p represents the distance from the photoevaporative source σ-Ori in parsecs (the projected distance).

We found values of FUV flux between 10^2 and 10^5 G_0 (see Fig. 5, top axis). We also estimated the FUV field strength produced by the other B-stars in the cluster and found that the FUV field is completely dominated by the multiple system σ-Ori. In Fig. 1 we showed the spatial distribution of disks in the cluster (circles) along with the massive O and B stars (gray stars). The color bar indicates the *total G_0* values (σ-Ori + B-stars) which as shown in Fig. B.1 mainly corresponds to the FUV field produced by σ-Ori.
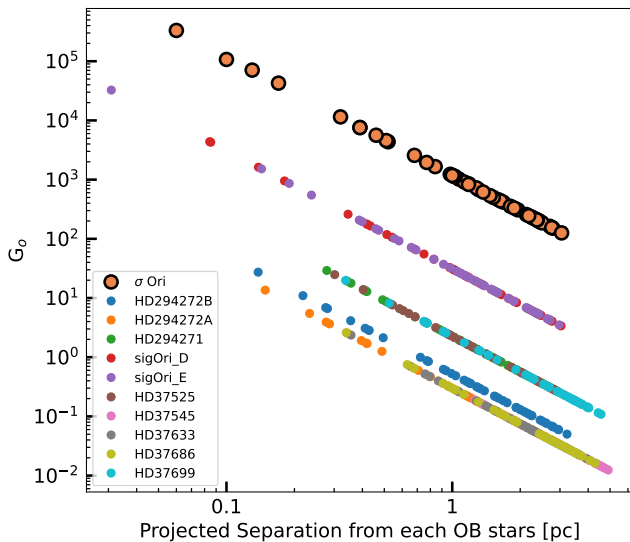

Fig. B.1: G_0 of O and B stars in the σ Orionis cluster. The FUV radiation is dominated by the central system σ-Ori.

Appendix C: Stellar and accretion parameters from previous works

We show on Table C.1 the stellar and accretion parameters of σ-Orionis sources from Manara et al. (2021). Overall, we found a good agreement (given our uncertainties) between our best-fit model and the results from Manara et al. (2021). SO518 and SO1153 are peculiar sources. SO518 seems to be an almost edge-on disk and, therefore, the estimate of its stellar parameters, particularly $\dot{M}_{\rm acc}$, is more uncertain (Alcalá et al. 2014). SO1153, on the other hand, is a strong accretor where the best-fit slab spectrum is much brighter than the photospheric template. Such strong accretors are problematic to fit, since the photospheric emission is veiled by the accretion emission, leading to large uncertainties in the best fit SpT (e.g., Calvet & Gullbring 1998), and many photospheric absorption lines are seen in emission. To obtain the final results for this source and for SO518 we had to constrain A_V to low values. Considering these caveats, we were able to obtain best-fit results compatible with the ones found by Manara et al. (2021).

Appendix D: Additional information on targets

Appendix D.1. ALMA observations

We obtained deeper ALMA Cycle 4 (C4) observations for disks in σ-Orionis. Fig. D.1 shows the comparison between ALMA observations from Ansdell et al. (2017, C3) and our new C4 observations. ALMA observations for our X-Shooter sample are reported in Table A.2. The list of ALMA non-detections is reported here (Table D.1). The data between both cycles agree very well. In general, the C4 fluxes are higher than in C3 by a factor $\sim$1.13 and the new detections have fluxes just at the level of the C3 upper limits (3σ). The C4 observations allow the detection of 6 new sources in the continuum. Furthermore, in an effort to establish more robust population statistics, especially for the gas, the higher sensitivity C4 data resulted in 13 new detections in ^{12}CO. The ^{12}CO fluxes are also reported in Table A.2. Continuum and ^{12}CO images are shown in Fig. D.2.

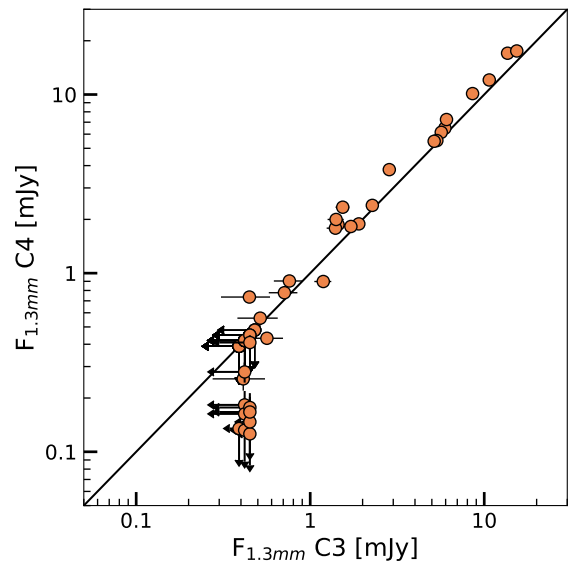

Fig. D.1: Comparison between ALMA fluxes from C3 and C4 for σ-Orionis sources. The arrows show 3σ upper limits.

Table A.1: σ-Orionis disk sample

Name	RA$_{2000}$ hh:mm:ss.s	Dec$_{2000}$ dd:mm:ss.s	Distance [pc]	$d_{\rm p}$ [pc]	Log G_o	Disk type
SO73	05:37:30.95	-02:23:42.8	$359.2^{-4.4}_{+4.2}$	2.32	2.34	–
SO299	05:38:00.97	-02:26:07.9	$355.5^{-4.4}_{+4.3}$	1.52	2.70	TD
SO341	05:38:06.74	-02:30:22.8	$409.0^{-4.4}_{+4.3}$	1.31	2.83	II
SO362	05:38:08.27	-02:35:56.3	$402.3^{-4.8}_{+4.6}$	1.07	3.01	II
SO397	05:38:13.20	-02:26:08.8	401.0	1.47	2.73	II
SO411	05:38:14.12	-02:15:59.8	$365.5^{-2.2}_{+2.2}$	2.28	2.35	TD
SO467	05:38:21.19	-02:54:11.1	$383.3^{-9.0}_{+8.6}$	2.13	2.41	–
SO490	05:38:23.58	-02:20:47.6	401.0	1.88	2.52	II
SO500	05:38:25.44	-02:42:41.3	$409.2^{-45.4}_{+37.2}$	0.98	3.09	II
SO518	05:38:27.26	-02:45:09.7	$399.0^{-4.0}_{+3.9}$	1.18	2.93	II
SO520	05:38:27.51	-02:35:04.2	$402.6^{-6.5}_{+6.3}$	0.52	3.64	II
SO540	05:38:29.16	-02:16:15.7	$406.0^{-3.6}_{+3.5}$	2.38	2.32	II
SO562	05:38:31.41	-02:36:33.8	401.0	0.39	3.88	II
SO563	05:38:31.58	-02:35:14.9	401.0	0.39	3.88	II
SO583	05:38:33.68	-02:44:14.2	401.0	1.01	3.06	II
SO587	05:38:34.06	-02:36:37.5	401.0	0.32	4.06	II
SO646	05:38:39.03	-02:45:32.2	$404.6^{-6.8}_{+6.6}$	1.13	2.96	II
SO662	05:38:40.27	-02:30:18.5	$401.2^{-3.4}_{+3.3}$	0.68	3.41	II
SO682	05:38:42.28	-02:37:14.8	$409.8^{-4.8}_{+4.7}$	0.17	4.63	II
SO687	05:38:43.02	-02:36:14.6	$412.8^{-4.3}_{+4.2}$	0.06	5.52	II
SO694	05:38:43.87	-02:37:06.8	$392.3^{-9.6}_{+9.2}$	0.13	4.85	–
SO697	05:38:44.23	-02:40:19.7	$404.5^{-2.4}_{+2.4}$	0.51	3.66	II
SO726	05:38:47.46	-02:35:25.2	$403.9^{-7.0}_{+6.8}$	0.10	5.03	II
SO736	05:38:48.04	-02:27:14.2	401.0	1.03	3.05	II
SO739	05:38:48.19	-02:44:00.8	$433.3^{-22.3}_{+20.3}$	1.02	3.06	II
SO774	05:38:52.01	-02:46:43.7	$403.3^{-3.4}_{+3.3}$	1.28	2.86	II
SO818	05:38:58.32	-02:16:10.1	$405.4^{-4.2}_{+4.1}$	2.37	2.32	TD
SO823	05:38:59.11	-02:47:13.3	401.0	1.37	2.79	II
SO844	05:39:01.37	-02:18:27.5	$415.5^{-3.8}_{+3.7}$	2.18	2.39	II
SO848	05:39:01.94	-02:35:02.9	$356.3^{-18.0}_{+16.3}$	0.46	3.75	II
SO859	05:39:02.98	-02:41:27.2	$407.9^{-6.6}_{+6.4}$	0.84	3.22	II
SO897	05:39:07.61	-02:32:39.1	401.0	0.77	3.29	TD
SO927	05:39:11.51	-02:31:06.5	$413.6^{-4.8}_{+4.7}$	1.0	3.07	II
SO984	05:39:18.83	-02:30:53.1	$409.6^{-3.2}_{+3.1}$	1.18	2.92	II
SO1036	05:39:25.20	-02:38:22.0	$395.0^{-3.5}_{+3.4}$	1.19	2.92	II
SO1075	05:39:29.35	-02:27:21.0	$390.0^{-8.6}_{+8.2}$	1.60	2.66	II
SO1152	05:39:39.38	-02:17:04.5	$398.6^{-3.9}_{+3.8}$	2.71	2.21	–
SO1153	05:39:39.82	-02:31:21.8	$396.6^{-4.3}_{+4.2}$	1.68	2.62	I
SO1154	05:39:39.83	-02:33:16.0	401.0	1.64	2.64	–
SO1155	05:39:39.90	-02:43:09.0	401.0	1.81	2.55	–
SO1156	05:39:40.17	-02:20:48.0	$403.8^{-2.6}_{+2.6}$	2.42	2.30	II
SO1248	05:39:51.73	-02:22:47.2	$398.4^{-7.9}_{+7.6}$	2.47	2.28	–
SO1260	05:39:53.63	-02:33:42.7	$386.3^{-6.4}_{+6.2}$	1.95	2.49	II
SO1266	05:39:54.21	-02:27:32.6	$399.1^{-11.0}_{+10.4}$	2.24	2.37	II
SO1267	05:39:54.29	-02:24:38.6	$400.5^{-5.3}_{+5.2}$	2.42	2.30	–
SO1274	05:39:54.60	-02:46:34.0	$407.3^{-2.7}_{+2.7}$	2.42	2.30	II
SO1327	05:40:01.96	-02:21:32.6	$397.7^{-5.8}_{+5.7}$	2.79	2.18	II
SO1361	05:40:08.89	-02:33:33.7	$406.0^{-4.0}_{+3.9}$	2.50	2.27	II
SO1362	05:40:09.33	-02:25:06.7	$399.4^{-10.7}_{+10.2}$	2.76	2.19	II
SO1369	05:40:12.87	-02:22:02.0	$402.5^{-2.5}_{+2.5}$	3.05	2.10	–

Table A.2: Stellar and accretion properties and disk masses

Name	SpT	T_{eff} [K]	A_V [mag]	$L_\star$ [$L_\odot$]	$\log L_{\text{acc}}$ [$L_\odot$]	$M_\star$ [$M_\odot$]	$\log \dot{M}_{\text{acc}}$ [$M_\odot$/yr]	F_{mm} [mJy]	M_{dust} [$M_\oplus$]	$F_{^{12}CO}$ [mJy]
SO73	M3	3410	1.0	0.2	-1.13	0.29	-7.89	0.53 ± 0.13	1.6 ± 0.4	< 66.0
SO299	M3.5	3300	0.2	0.22	-2.62	0.24	-9.26	1.01 ± 0.14	3.0 ± 0.4	< 66.0
SO341	M0	3900	0.8	0.55	-1.18	0.59	-8.14	1.19 ± 0.13	3.5 ± 0.1	<34.35
SO362	M3	3410	1.4	0.6	-0.7	0.3	-7.23	0.56 ± 0.13	1.6 ± 0.1	<34.02
SO397	M4.5	3085	0.0	0.24	-2.62	0.19	-9.06	< 0.4	< 1.6	< 69.0
SO411	G4	5516	0.6	11.67	-0.4	2.65	-7.66	5.16 ± 0.13	17.1 ± 0.1	130.35 ± 18.02
SO467	M5.5	2920	0.3	0.07	-3.18	0.1	-9.57	0.61 ± 0.13	2.1 ± 0.5	< 66.0
SO490	M5.5	2920	0.0	0.1	-3.01	0.13	-9.41	< 0.4	< 1.6	< 72.0
SO500	M6	2860	0.0	0.02	-3.84	0.06	-10.22	< 0.4	< 1.6	< 63.0
SO518	K6	4115	1.6	0.48	-0.69	0.8	-7.86	0.52 ± 0.13	2.1 ± 0.1	96.61 ± 18.57
SO520	M4.5	3085	0.1	0.23	-2.01	0.18	-8.45	0.52 ± 0.14	2.0 ± 0.5	< 69.0
SO540	K6	4115	0.5	0.57	-1.84	0.77	-8.96	10.69 ± 0.29	46.4 ± 0.3	1306.92 ± 45.33
SO562	M5.5	2920	0.3	0.26	-1.44	0.15	-7.7	0.71 ± 0.13	2.9 ± 0.1	<33.66
SO563	M0	3900	0.6	0.36	-1.27	0.64	-8.36	0.18 ± 0.04	0.7 ± 0.1	< 33.0
SO583	K4	4375	1.0	4.06	-0.69	1.18	-7.62	1.9 ± 0.13	7.1 ± 0.1	68.95 ± 12.52
SO587	M4.5	3085	0.0	0.35	-3.91	0.21	-10.31	< 0.1	< 0.4	< 33.6
SO646	M3.5	3300	0.0	0.12	-2.9	0.25	-9.66	< 0.4	< 1.6	< 69.0
SO662	K7	4020	0.3	0.68	-3.79	0.64	-10.77	1.54 ± 0.14	8.8 ± 0.2	<33.99
SO682	M0	3900	0.7	0.76	-2.02	0.57	-8.89	0.41 ± 0.14	1.0 ± 0.1	<30.78
SO687	M1	3720	0.8	0.73	-1.21	0.44	-7.94	0.28 ± 0.04	1.1 ± 0.1	< 32.1
SO694	M5.5	2920	0.1	0.16	-2.51	0.12	-8.82	0.61 ± 0.14	2.2 ± 0.5	< 69.0
SO697	K6	4115	0.2	0.97	-3.11	0.67	-10.05	0.16 ± 0.04	0.6 ± 0.1	< 33.9
SO726	M0	3900	0.6	0.56	-2.19	0.59	-9.15	0.18 ± 0.04	0.7 ± 0.1	< 33.4
SO736	K7	4020	0.1	1.49	-1.48	0.55	-8.23	0.45 ± 0.14	2.8 ± 0.1	<35.88
SO739	M6.5	2815	0.1	0.1	-3.06	0.1	-9.35	0.52 ± 0.14	2.3 ± 0.6	< 69.0
SO774	K7	4020	0.0	0.49	-2.75	0.7	-9.84	0.76 ± 0.14	3.4 ± 0.1	104.2 ± 15.91
SO818	K7	4020	0.4	0.29	-2.11	0.78	-9.36	1.97 ± 0.15	7.5 ± 0.6	514.0 ± 58.0
SO823	K7	4020	1.5	0.32	-2.43	0.77	-9.66	0.17 ± 0.04	0.6 ± 0.1	< 32.2
SO844	M1	3720	0.7	0.62	-1.37	0.44	-8.14	2.85 ± 0.14	15.3 ± 0.1	172.14 ± 16.73
SO848	M4	3190	0.0	0.02	-3.51	0.17	-10.47	0.52 ± 0.14	1.5 ± 0.4	< 66.0
SO859	M3	3410	0.6	0.41	-1.72	0.29	-8.31	2.49 ± 0.14	9.7 ± 0.6	< 69.0
SO897	K6	4115	0.6	0.85	-1.34	0.7	-8.33	1.71 ± 0.14	6.8 ± 0.1	78.54 ± 15.28
SO927	M0	3900	0.6	0.33	-1.92	0.65	-9.03	1.41 ± 0.15	8.0 ± 0.1	75.95 ± 10.77
SO984	K7	4020	0.1	0.72	-3.5	0.64	-10.46	6.07 ± 0.15	28.4 ± 0.1	276.62 ± 30.32
SO1036	M0	3900	0.7	0.53	-0.89	0.59	-7.86	5.94 ± 0.25	23.6 ± 0.2	233.88 ± 31.42
SO1075	M3	3410	0.6	0.14	-1.38	0.3	-8.22	1.48 ± 0.15	5.2 ± 0.5	165.0 ± 33.0
SO1152	M0	3900	0.8	0.61	-1.26	0.58	-8.19	8.57 ± 0.29	37.5 ± 0.3	748.6 ± 35.8
SO1153	K5	4210	1.5	0.33	0.02	0.9	-7.3	13.62 ± 0.27	62.5 ± 0.2	746.87 ± 37.91
SO1154	K7	4020	1.8	0.08	-0.78	0.62	-8.19	1.44 ± 0.15	7.0 ± 0.1	<33.96
SO1155	K4	4375	0.6	1.45	-0.92	0.86	-7.94	0.41 ± 0.04	0.7 ± 0.1	< 34.4
SO1156	K6	4115	0.4	0.66	-1.26	0.74	-8.33	5.66 ± 0.15	23.4 ± 0.2	263.26 ± 22.57
SO1248	M5.5	2920	0.0	0.18	-3.3	0.13	-9.6	0.79 ± 0.15	2.9 ± 0.6	< 72.0
SO1260	M4	3190	0.0	0.15	-1.94	0.19	-8.53	< 0.4	< 1.5	< 69.0
SO1266	M4.5	3085	0.0	0.07	-4.76	0.15	-11.36	< 0.5	< 1.7	< 72.0
SO1267	M1	3720	0.6	0.76	-1.85	0.43	-8.57	2.27 ± 0.15	9.0 ± 0.1	170.01 ± 18.73
SO1274	K7	4020	0.0	0.68	-0.98	0.64	-7.95	15.38 ± 0.42	67.9 ± 0.4	1018.3 ± 38.63
SO1327	M4.5	3085	0.1	0.33	-1.91	0.21	-8.32	1.63 ± 0.16	6.0 ± 0.6	< 75.0
SO1361	M1	3720	0.5	0.47	-0.61	0.46	-7.46	5.34 ± 0.15	21.2 ± 0.1	208.19 ± 25.69
SO1362	M5.5	2920	0.0	0.1	-2.96	0.13	-9.37	1.02 ± 0.15	3.8 ± 0.6	< 72.0
SO1369	K7	4020	0.0	1.26	-1.45	0.57	-8.24	1.4 ± 0.15	6.8 ± 0.1	55.79 ± 14.13

Table C.1: Comparison between our best fit results and the ones of Manara et al. (2021) for the targets SO518, SO583, and SO1153.

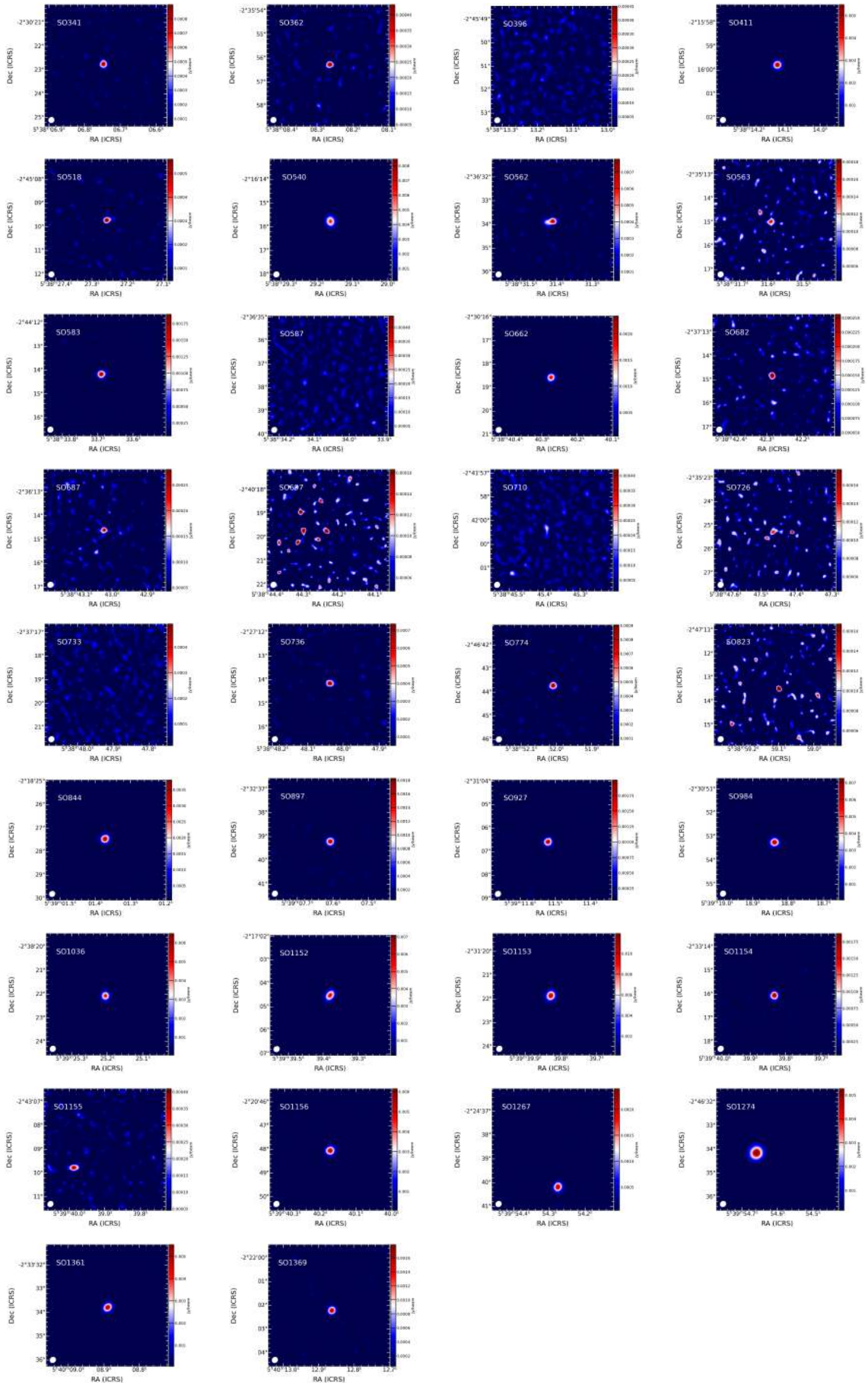| Name	SpT	A_V	$L_\star$	$\log L_{\mathrm{acc}}$	$M_\star$	$\log \dot{M}_{\mathrm{acc}}$
SO518	K6	1.6	0.48	-0.69	0.80	-7.86
SO518 Manara et al. (2021)	K7	1.0	0.24	-1.22	0.81	-8.53
SO583	K4	1.0	4.06	-0.69	1.18	-7.62
SO583 Manara et al. (2021)	K5	0.4	3.61	-0.30	1.09	-7.21
SO1153	K5	1.5	0.33	0.02	0.90	-7.30
SO1153 Manara et al. (2021)	K7	0.1	0.17	-0.88	0.76	-8.24

Fig. D.2: Continuum images at 1.33 mm of the 34 disks sampled by ALMA in Cycle 4, ordered by source name.
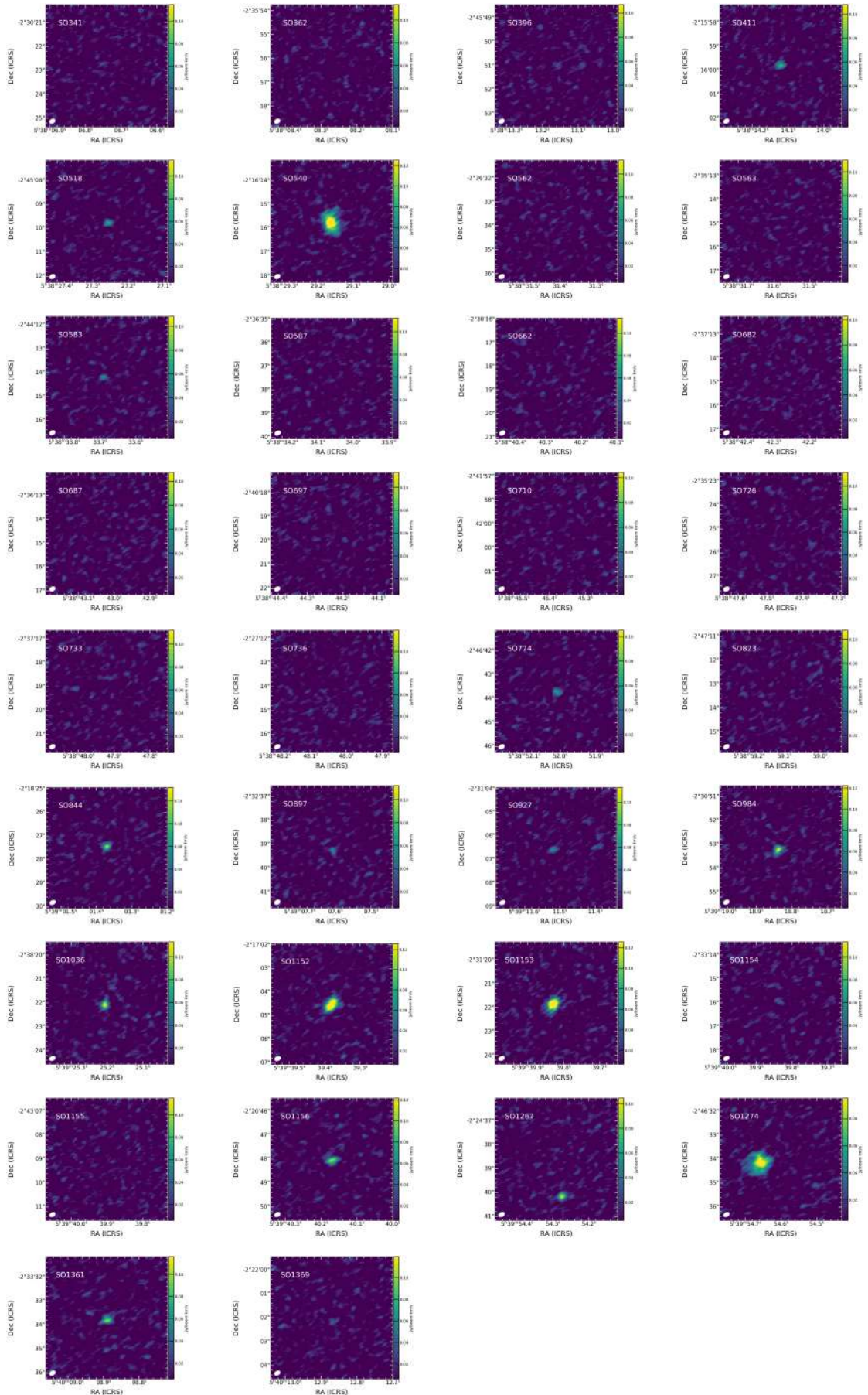
Fig. D.2: (cont.) ^{12}CO Moment 0 maps of the 34 disks sampled by ALMA in Cycle 4, ordered by source name.

Table D.1: ALMA non-detections

Name	RA$_{2000}$ hh:mm:ss.s	Dec$_{2000}$ dd:mm:ss.s	Distance [pc]	d_p [pc]	Log G_o	Disk type	M_{dust} [M$_\oplus$]
SO247	05:37:54.86	-02:41:09.2	$392.2^{+10.0}_{-9.5}$	1.54	2.69	II	<1.42
SO254	05:37:55.60	-02:33:05.3	$373.4^{+41.3}_{-33.8}$	1.37	2.79	II	<1.28
SO271	05:37:57.46	-02:38:44.4	$396.0^{+20.2}_{-18.4}$	1.4	2.78	II	<1.43
SO300	05:38:01.07	-02:45:38.0	$401.0^{+16.7}_{-15.0}$	1.7	2.61	–	<1.5
SO327	05:38:05.52	-02:35:57.1	$392.3^{+59.3}_{-45.6}$	1.12	2.97	II	<1.44
SO396	05:38:13.16	-02:45:51.0	$404.6^{+3.9}_{-3.8}$	1.49	2.73	II	<0.41
SO435	05:38:17.78	-02:40:50.1	401.0	0.97	3.1	II	<1.48
SO451	05:38:18.86	-02:51:38.8	$409.2^{+6.1}_{-5.9}$	2.02	2.46	–	<1.55
SO462	05:38:20.50	-02:34:09.0	$379.7^{+11.7}_{-11.0}$	0.7	3.38	II	<1.34
SO482	05:38:23.08	-02:36:49.4	$403.3^{+22.3}_{-20.1}$	0.64	3.45	–	<1.57
SO485	05:38:23.33	-02:25:34.6	$360.7^{+10.2}_{-9.6}$	1.23	2.89	II	<1.23
SO514	05:38:26.84	-02:38:46.1	$351.5^{+15.9}_{-14.6}$	0.54	3.61	II	<1.15
SO537	05:38:28.97	-02:48:47.3	$416.7^{+38.3}_{-32.4}$	1.62	2.65	–	<1.62
SO598	05:38:34.60	-02:41:08.8	$400.4^{+7.6}_{-7.3}$	0.67	3.42	II	<1.51
SO657	05:38:39.76	-02:32:20.3	$402.8^{+81.1}_{-57.8}$	0.45	3.76	–	<1.57
SO663	05:38:40.54	-02:33:27.6	$405.5^{+9.0}_{-8.7}$	0.32	4.05	–	<1.57
SO674	05:38:41.60	-02:30:28.9	$383.8^{+6.6}_{-6.4}$	0.62	3.48	–	<1.47
SO707	05:38:45.28	-02:37:29.3	$405.5^{+18.2}_{-16.7}$	0.18	4.58	–	<1.62
SO710	05:38:45.38	-02:41:59.4	$401.0^{+19.4}_{-16.8}$	0.7	3.38	II	<0.4
SO723	05:38:47.19	-02:34:36.8	$392.0^{+9.2}_{-8.8}$	0.17	4.59	II	<1.58
SO733	05:38:47.92	-02:37:19.2	$411.4^{+6.7}_{-6.5}$	0.18	4.54	II	<0.43
SO738	05:38:48.10	-02:28:53.6	$377.2^{+24.0}_{-21.3}$	0.79	3.28	–	<1.4
SO750	05:38:49.29	-02:23:57.6	$425.0^{+31.0}_{-27.0}$	1.5	2.72	–	<1.85
SO754	05:38:49.70	-02:34:52.6	$392.6^{+12.6}_{-11.8}$	0.19	4.51	–	<1.52
SO762	05:38:50.61	-02:42:42.9	$394.0^{+15.5}_{-14.4}$	0.79	3.28	–	<1.53
SO827	05:38:59.23	-02:33:51.4	$410.7^{+8.4}_{-8.0}$	0.5	3.67	II	<1.67
SO865	05:39:03.57	-02:46:27.0	$399.5^{+7.3}_{-7.1}$	1.33	2.82	II	<1.61
SO866	05:39:03.87	-02:20:08.2	$379.7^{+13.7}_{-12.8}$	1.83	2.54	II	<1.48
SO871	05:39:04.59	-02:41:49.4	$429.4^{+12.8}_{-12.1}$	0.95	3.11	II	<1.84
SO908	05:39:08.78	-02:31:11.5	$383.6^{+8.1}_{-7.8}$	0.86	3.2	II	<1.51
SO936	05:39:13.08	-02:37:50.9	$401.0^{+85.4}_{-63.3}$	0.85	3.21	–	<1.64
SO967	05:39:15.83	-02:36:50.7	$396.0^{+8.6}_{-8.3}$	0.9	3.16	II	<1.58
SO1050	05:39:26.33	-02:28:37.7	$389.5^{+11.5}_{-10.8}$	1.44	2.75	–	<1.58
SO1182	05:39:43.19	-02:32:43.3	$390.0^{+9.5}_{-9.1}$	1.7	2.61	–	<1.57
SO1193	05:39:44.51	-02:24:43.2	$439.8^{+23.5}_{-21.2}$	2.4	2.31	–	<2.01
SO1230	05:39:49.45	-02:23:45.9	$413.6^{+10.8}_{-10.3}$	2.44	2.29	–	<1.77
SO1268	05:39:54.33	-02:37:18.9	$441.6^{+45.4}_{-37.7}$	2.24	2.37	TD	<2.03
SO1338	05:40:04.54	-02:36:42.1	$419.7^{+77.5}_{-56.6}$	2.44	2.3	–	<1.84
SO1344	05:40:05.26	-02:30:52.3	$394.3^{+18.1}_{-16.6}$	2.38	2.32	–	<1.62

Appendix D.2. Gaia observations

Gaia information for our X-Shooter sample is listed on Table D.2. Information on parallaxes (ϖ), proper motions (μ_α, μ_β), and RUWE values are provided for each source.

Appendix E: Plots of the Balmer jump fits

Here, we present the best fit of the X-Shooter spectra of our sample obtained following Manara et al. (2013a) and described in Sect. 4.1. We show the Balmer jump region of the spectra for each target.

Table D.2: Information on distances from Gaia for our X-Shooter sample

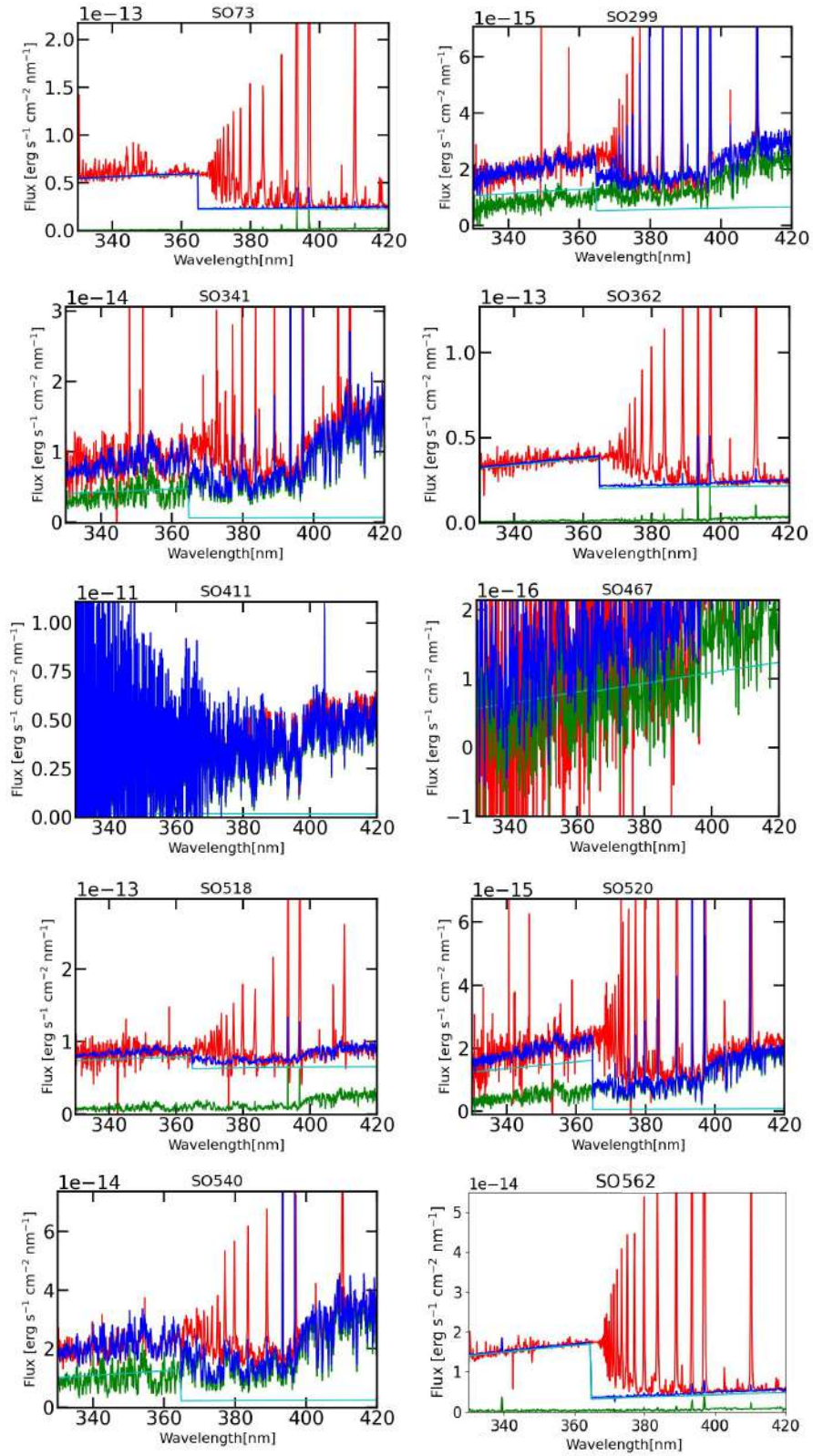| Name	ϖ [mas]	σ_ϖ [mas]	μ_α [mas/yr]	μ_δ [mas/yr]	RUWE
SO73	2.7843	0.0333	1.757 ± 0.034	-1.313 ± 0.027	1.14
SO299	2.8126	0.0344	1.749 ± 0.036	-1.41 ± 0.028	0.99
SO341	2.4451	0.0259	1.334 ± 0.028	-0.529 ± 0.021	1.1
SO362	2.4859	0.0291	1.057 ± 0.034	-0.615 ± 0.026	1.08
SO397	2.4075	0.2217	0.816 ± 0.193	0.846 ± 0.161	2.45
SO411	2.736	0.0164	1.923 ± 0.014	-1.37 ± 0.013	0.83
SO467	2.6087	0.0601	1.237 ± 0.055	-1.306 ± 0.049	1.03
SO490	3.8006	0.6852	-0.999 ± 0.671	-3.064 ± 0.571	7.94
SO500	2.4437	0.2443	0.977 ± 0.293	-0.944 ± 0.229	1.1
SO518	2.5064	0.025	1.191 ± 0.027	-0.895 ± 0.022	1.2
SO520	2.4839	0.0397	1.409 ± 0.039	-0.571 ± 0.032	1.0
SO540	2.4629	0.0216	0.316 ± 0.019	0.709 ± 0.017	1.16
SO563	7.7206	0.8106	3.868 ± 0.767	5.7 ± 0.633	35.66
SO583	2.4699	0.223	1.07 ± 0.238	-0.485 ± 0.191	19.86
SO587	2.1903	0.2054	0.298 ± 0.202	0.855 ± 0.165	6.77
SO646	2.4714	0.0409	1.243 ± 0.044	-0.72 ± 0.037	1.04
SO662	2.4925	0.0208	0.871 ± 0.018	-0.61 ± 0.017	1.12
SO682	2.4402	0.0284	1.072 ± 0.027	-0.349 ± 0.022	1.22
SO687	2.4226	0.0251	1.566 ± 0.026	0.132 ± 0.022	1.13
SO694	2.5492	0.0612	1.733 ± 0.06	-1.114 ± 0.05	1.12
SO697	2.4723	0.0148	1.459 ± 0.014	-1.009 ± 0.012	1.03
SO726	2.4761	0.0425	2.21 ± 0.045	0.097 ± 0.04	1.14
SO736	2.5267	0.0608	1.456 ± 0.054	0.147 ± 0.05	3.32
SO739	2.3081	0.1132	1.368 ± 0.125	-0.946 ± 0.095	0.98
SO774	2.4796	0.0205	1.63 ± 0.021	-1.074 ± 0.016	1.11
SO818	2.4665	0.0253	0.746 ± 0.024	0.4 ± 0.021	1.1
SO823	2.2249	0.058	0.845 ± 0.062	0.104 ± 0.053	1.46
SO844	2.4067	0.0216	1.704 ± 0.023	-0.052 ± 0.02	1.1
SO848	2.8064	0.1347	1.689 ± 0.128	-0.225 ± 0.119	1.08
SO859	2.4517	0.0389	1.561 ± 0.037	-0.715 ± 0.033	1.04
SO897	2.6239	0.0517	1.588 ± 0.049	-0.922 ± 0.044	3.28
SO927	2.4178	0.0276	1.832 ± 0.026	-0.316 ± 0.024	1.27
SO984	2.4412	0.0188	1.808 ± 0.021	-0.654 ± 0.017	1.09
SO1036	2.5318	0.0221	1.843 ± 0.018	-0.349 ± 0.018	1.19
SO1075	2.5638	0.0554	1.701 ± 0.053	-0.122 ± 0.047	1.18
SO1152	2.5091	0.0245	2.105 ± 0.024	-0.033 ± 0.02	1.3
SO1153	2.5212	0.0268	1.798 ± 0.023	-0.094 ± 0.02	1.23
SO1154	2.4985	0.0797	2.113 ± 0.075	-0.824 ± 0.068	1.4
SO1156	2.4765	0.0159	2.44 ± 0.017	-0.255 ± 0.014	1.08
SO1248	2.51	0.0486	2.221 ± 0.049	-0.183 ± 0.042	1.09
SO1260	2.5888	0.0419	2.259 ± 0.039	-0.318 ± 0.032	1.03
SO1266	2.5055	0.0673	2.004 ± 0.062	-0.496 ± 0.053	0.98
SO1267	2.4967	0.0325	2.149 ± 0.03	-0.193 ± 0.026	1.29
SO1274	2.455	0.0164	2.166 ± 0.017	-0.781 ± 0.014	1.01
SO1327	2.5147	0.0363	2.336 ± 0.037	0.018 ± 0.03	1.01
SO1361	2.4632	0.0239	2.253 ± 0.019	-0.254 ± 0.018	1.16
SO1362	2.5041	0.0656	2.228 ± 0.058	-0.39 ± 0.052	1.08
SO1369	2.4843	0.0153	-2.476 ± 0.014	-4.16 ± 0.012	0.97

Fig. E.1: Best fit for the Balmer continuum region for targets in the σ-Orionis cluster, ordered by source name.
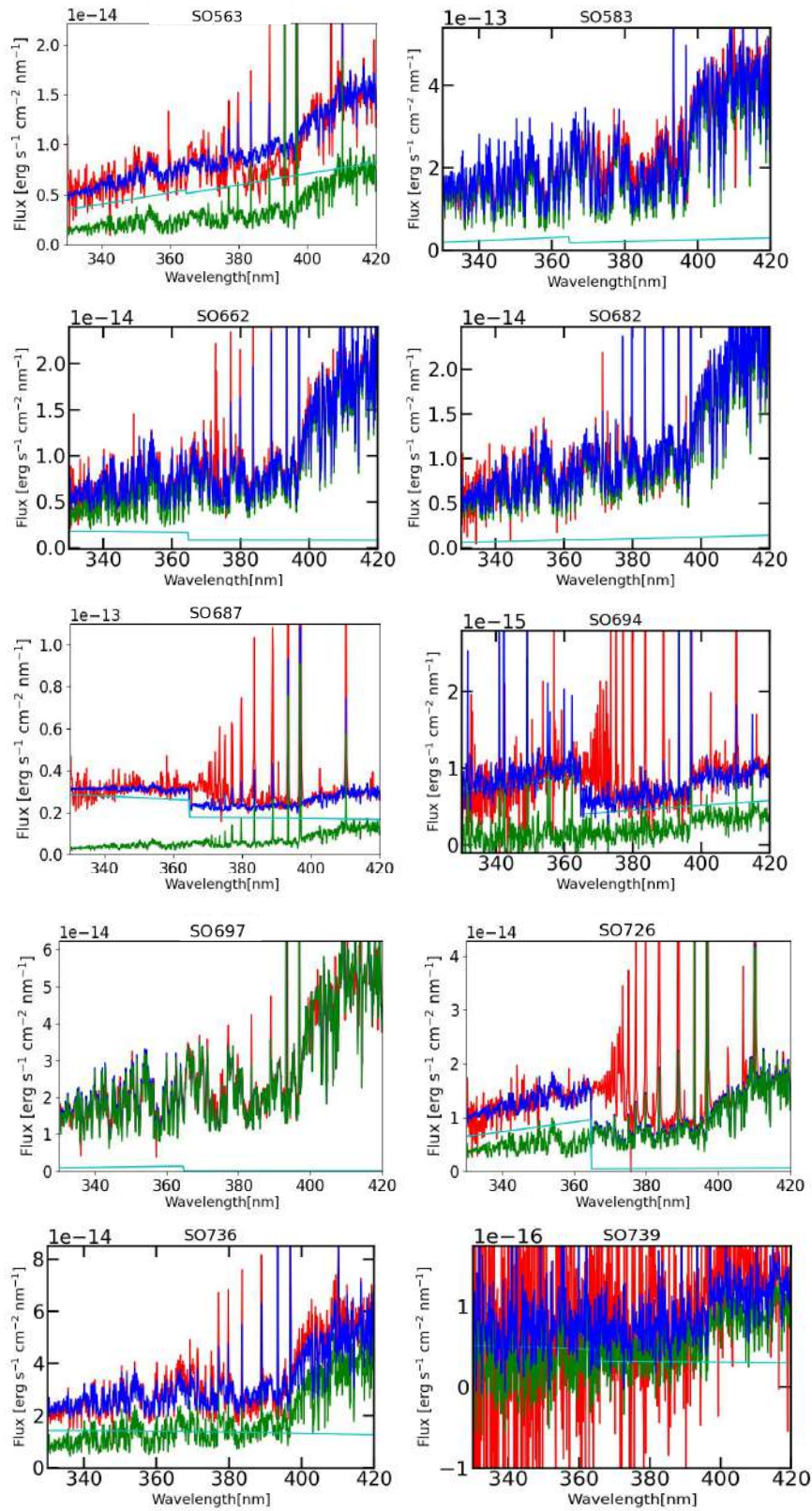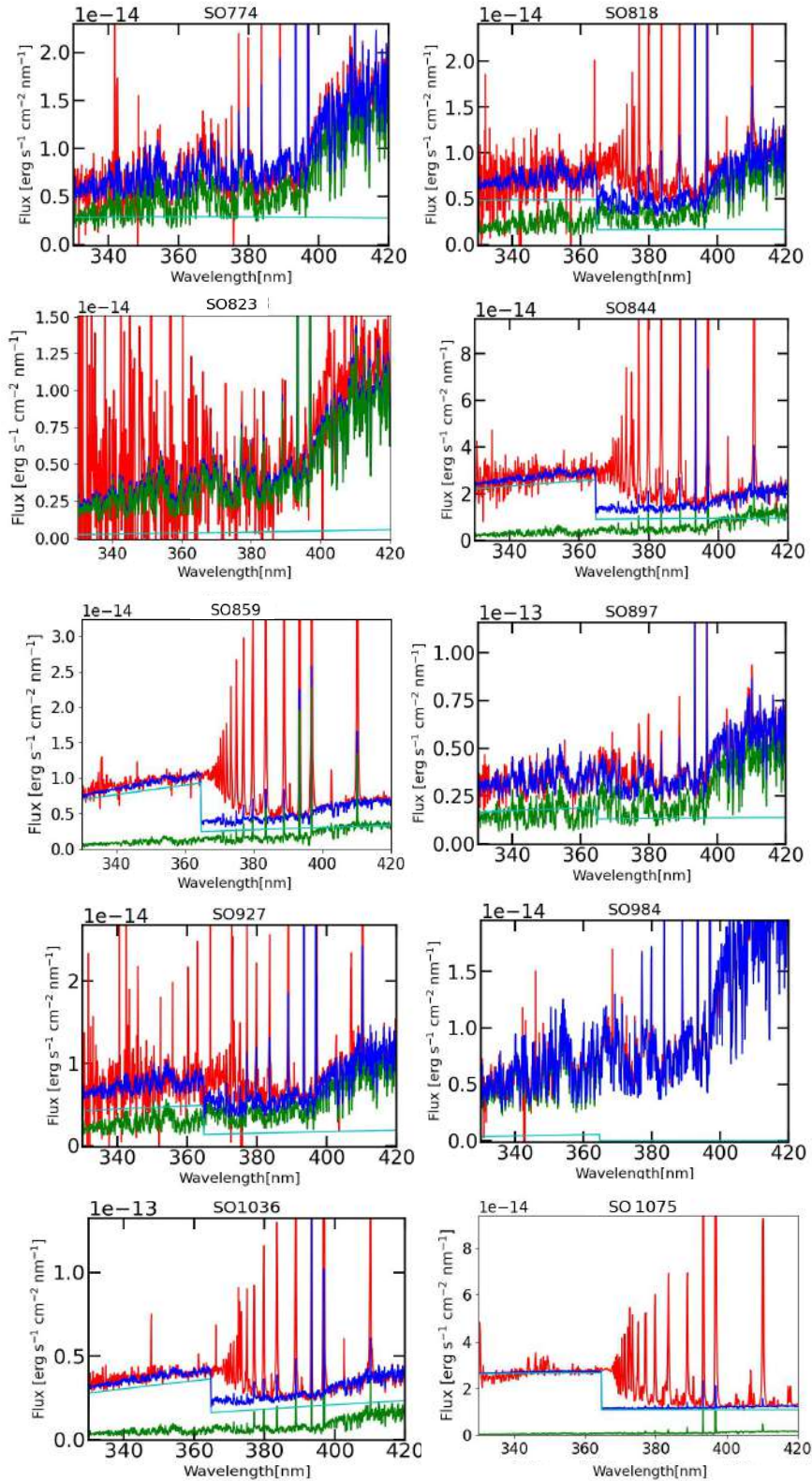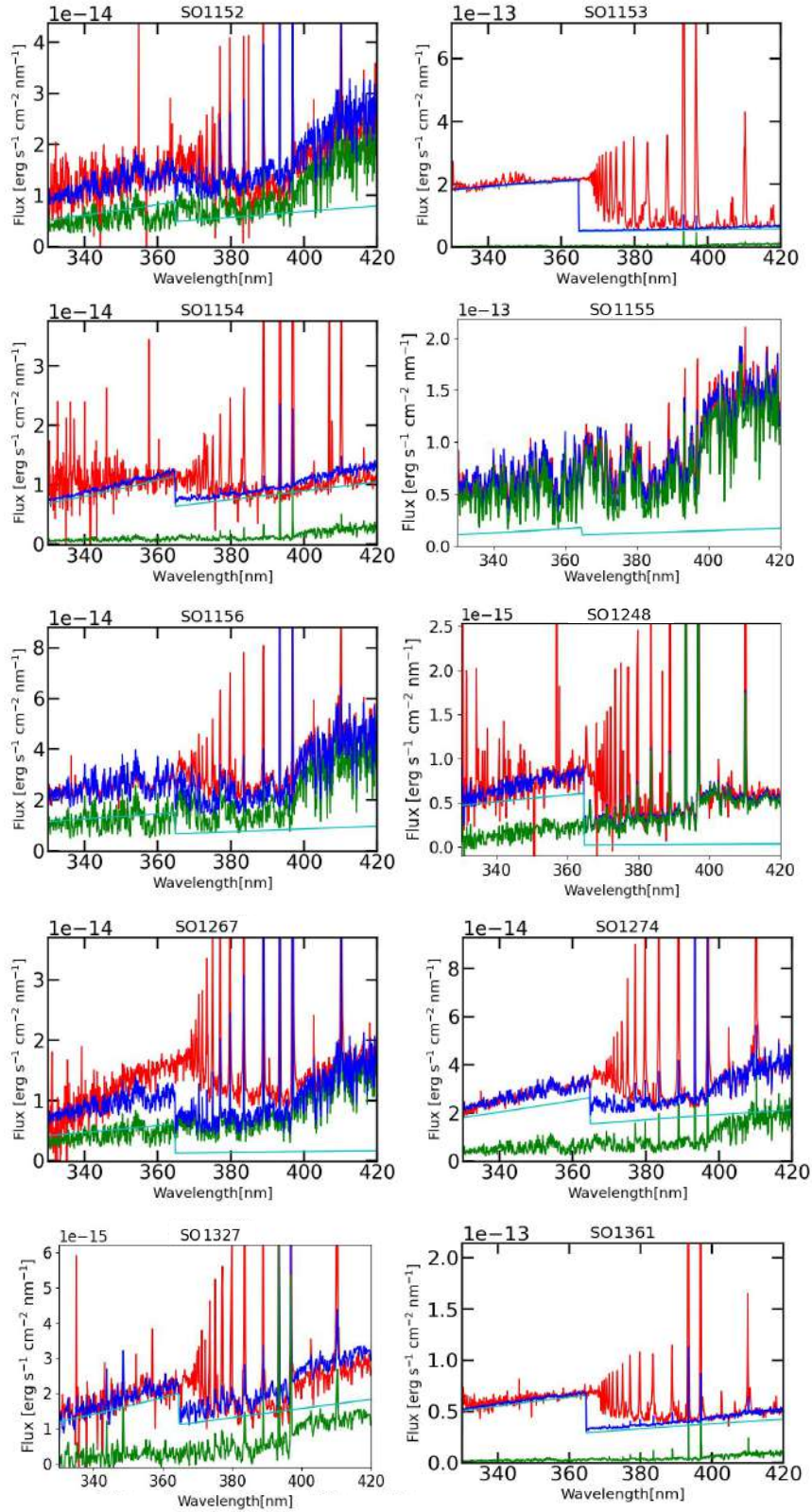
Fig. E.1: (cont.) Best fit for the Balmer continuum region for targets in the σ-Orionis cluster, ordered by source name.

Fig. E.1: (cont.) Best fit for the Balmer continuum region for targets in the σ-Orionis cluster, ordered by source name.

Fig. E.1: (cont.) Best fit for the Balmer continuum region for targets in the σ-Orionis cluster, ordered by source name.

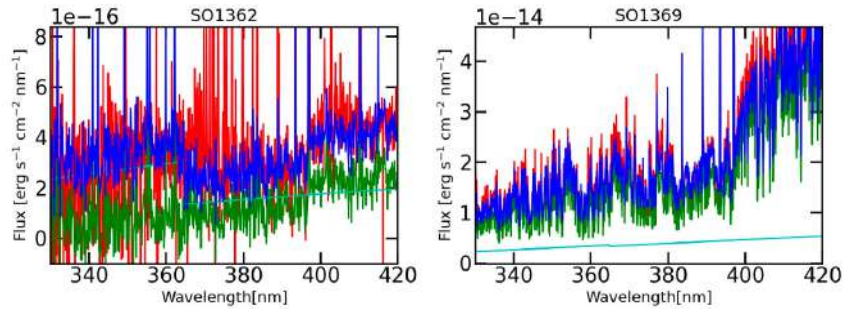Fig. E.1: (cont.) Best fit for the Balmer continuum region for targets in the σ-Orionis cluster, ordered by source name.